The Design of an Anti-Aliasing Filter for the Next Generation Digitiser

Edroy Theunissen

Supervisor: Dr. WPF Schonken
Co-Supervisor: Mr J.A Malan

Faculty of Engineering and the Built Environment
University of Cape Town

Submitted to the Department of Electrical Engineering at the University of Cape Town in partial fulfilment of the academic requirements for a Master of Science degree in Electrical Engineering.

June 2022

Declaration

I know the meaning of plagiarism and declare that all of the work in the dissertation, save for that which is properly acknowledged, is my own. This thesis/dissertation has been submitted to the Turnitin module (or equivalent similarity and originality checking software) and I confirm that my supervisor has seen my report and any concerns revealed by such have been resolved with my supervisor.

Signed by candidate

. . . .

Edroy Theunissen
June 2022

Dedication

I would like to dedicate this dissertation to my amazing wife, Carnesche and our sons Aaron and Ethan.

Acknowledgements

I wish to sincerely thank:

- Dr. WPF Schonken, my supervisor, for his support and guidance during the critical phases of my research.
- Sias Malan, my co-supervisor and manager, thank you for your constant mentorship and immeasurable support during my research and studies.
- All my collegues at South African Radio Astronomy Observatory (SARAO) for their support and assistance.
- The South African Radio Astronomy Observatory (SARAO) and National Research Foundation (NRF) for funding my studies.
- My family, for their unwavering motivation and support throughout my studies.

Abstract

MeerKAT, is a 64-element radio astronomy antenna array which has been recently constructed in the Northern Cape Province of South Africa. It serves as South Africa's contribution towards the international Square Kilometre Array (SKA) project. The MeerKAT array has been designed to observe radio signals produced by celestial sources at UHF-Band, L-Band, S-Band and X-Band frequencies.

The first phase of the construction included the design, development and integration of the UHF-Band, L-Band and S-band Receivers, whilst the X-band design has been superseded by the incorporation of the next phase of the SKA international project. In preparation of the next the roll-out, research is required to determine optimal wideband filter topologies suitable for direct digitisation of signal frequencies over the frequency range of 3-6 GHz.

In this thesis, exploration of suitable wideband planar filters is performed, noting those with an improved out-of-band rejection. The outcome of the investigation leads into the design and development of the suitable wideband planar filter based on key performance specifications. The performance of the manufactured wideband planar filter is then compared to the theoretical design, and validated against the key performance requirements.

Contents

List of Figures

List of Tables

1 Introduction **1**

2 Background Theory **8**

3 Planar Filter Technologies **24**

4 Design of Anti-aliasing Filter **44**

5 Conclusions and Recommendations **62**

Nomenclature

1 Acronyms

ADC	Analogue to Digital Converter
dBm	Decibel, relative to 1 mW
DSP	Digital Signal Processor (or processing)
FPGA	Field Programmable Gate Array
Gsps	Giga-samples per second
Hz	Hertz
I/O	Inputs/Outputs
IF	Intermediate Frequency
km	Kilometre
LCP	Liquid Crystal Polymer
LTCC	Low-temperature Co-fired Ceramic
PCB	Printed Circuit Board
RF	Radio Frequency
SARAO	South African Radio Astronomy Observatory
SKA	Square Kilometre Array
UWB	Ultra-wideband

Chapter 1

Introduction

Radio Astronomy can be dated back to 1932, where Karl Jansky coincidentally discovered natural radio emissions emanating from celestial sources within our Galaxy. Jansky's discovery was later validated in 1938 by a Dutch amateur radio operator and professional radio engineer Grote Reber, where he successfully built a parabolic reflector antenna in his backyard to detect and map the universe at 160 MHz [1].

One of the major parts that comprises a radio telescope is a receiver. The radio emissions detected by the antenna are measured by the receiver as broadband noise, and are nearly indistinguishable from noise generated from electronics. Various techniques are used to try and minimise the effects thereof, one of which is to cool the amplifiers and front-end electronic equipment of the receiver to cryogenic temperatures. Furthermore the receiver band-limits, or filters, the broadband noise, all of which contributes to a lower system noise temperature which is a critical performance parameter of a radio telescope.

The objective of this thesis is to investigate and design an ultra-wideband filter operating at 4.5 GHz with a bandwidth of 2.5 GHz. This work closely follows on from [2] and [3] where an in-depth system analysis and design was presented for digitisation options available for use in the receiver architecture of the MeerKAT telescope operating at the extended X-band frequency range of 8 to 14.5 GHz. The work presented in this thesis carries on from the overall system design, where it focuses on the design of an ultra-wideband filter which will be used in the system as an anti-aliasing filter.

1.1 Background

1.1.1 MeerKAT – System Overview

The MeerKAT Radio Telescope, as it stands, is a 64 receptor, offset Gregorian radio astronomy antenna array located near Carnavon in the Northern Cape Province of Southern Africa. This project was designed and built as a technology demonstrator which would serve as South Africa's contribution towards in the international project called the Square Kilometre Array (SKA) [4] [5]. The goal of the international project is to construct the world's largest radio telescope which will have an overall antenna collecting area of one square kilometer.

Figure 1.1: MeerKAT array as it stands in Carnavon [6].

The major components of a single antenna structure used on the MeerKAT project consists of:

- A main- and sub-reflector; which intercepts the electromagnetic waves,
- A receiver system; which converts the electromagnetic wave to electrical signals where they are amplified by cryogenically cooled low-noise amplifiers (LNA), and
- A digitiser; where the electrical signals fed from the receiver system gets digitised.

The MeerKAT telescope can accommodate four independent receivers, but currently only consists of three receivers which operate at L-Band, UHF-Band and S-Band respectively. They are physically positioned on the receiver indexer, which is a rotating mechanical support platform, which allows the appropriate receiver and digitiser to be automatically moved into the antenna focus position, depending on the desired observation frequency [7]. The initial plan was that a X-Band receiver be designed and built for the vacant position on the receiver indexer, but has since been superseded by the incorporation of the next phase of the SKA international project. The next phase of the SKA international project, termed SKA1-Mid, will consist of 133 offset-Gregorian dishes which will be integrated with the existing 64 MeerKAT dishes [8] resulting in the array achieving baselines of up to 150 km covering frequencies from 350 MHz to 16 GHz [9].

1.1.2 MeerKAT Digitiser - System Overview

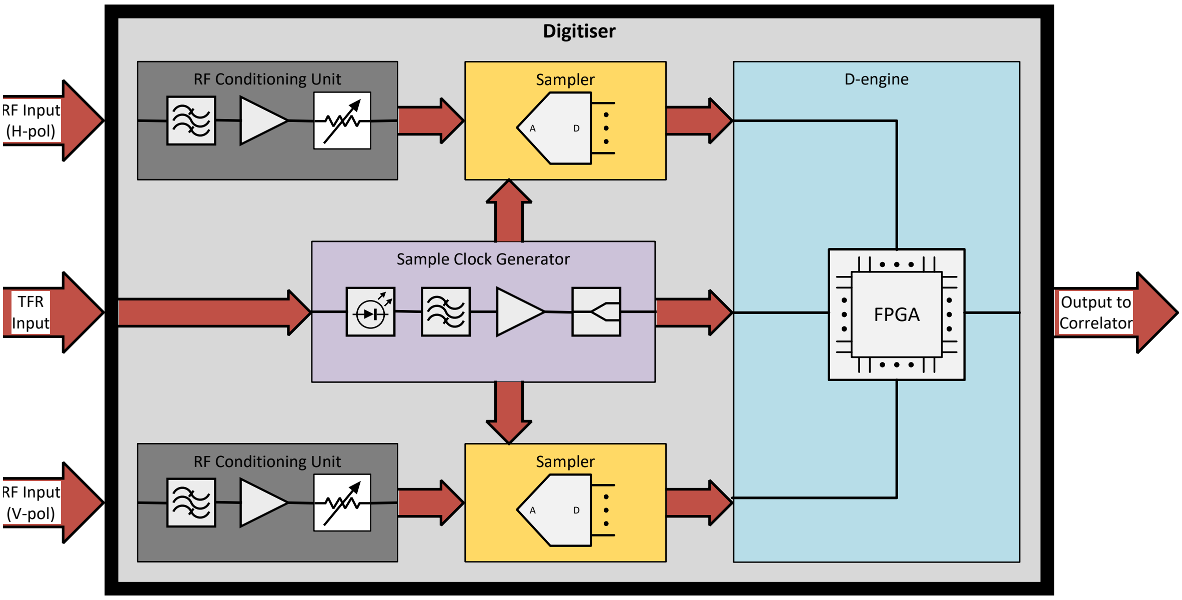

Figure 1.2: Digitiser signal path (adapted from [10]).

The main function of the digitiser is to digitise the analogue RF signal provided by the receivers. RF signals from both polarisations (H-pol and V-pol respectively) of each feed enter the appropriate digitiser and get conditioned via an analogue RF conditioning unit before entering the ADC. The RF conditioning unit filters and amplifies the signal before entering the ADC. Filtering is done in such a manner that aliasing of noise is prevented. A brief discussion about the concept of aliasing is addressed in Section 1.2.2.

Further functionality of the RF conditioning unit is to provide adjustable gain to improve telescope operational dynamic range. An ultra-high-speed ADC samples the conditioned RF based on a sample clock that is provided by the Timing and Frequency Reference (TFR) subsystem.

The D-engine receives the digitised data from the ADC where it is then packetised and transported to the Correlator data switch via Ethernet fibre optic links. All data products are time stamped with the digitiser local time which is derived from a 1 pulse-per-second (1PPS) signal provided by the TFR subsystem via analogue fibre.

1.2 Project Overview

1.2.1 Next Generation Digitiser

The development of the next generation digitiser is considered to be a technology development project, which can be used to digitise analogue input signals from high frequency receivers.

It was proposed by [2] and [3] that the next generation digitiser makes use of a single stage down-converted heterodyne receiver capable of down-converting high frequency signals to an intermediate frequency (IF) of 4.5 GHz which can be sampled at 6 Gsps. It is further proposed in [2] that the ADC selected for the design should be the Teledyne (e2V) EV12AQ600. It is a 12-bit, quad channel ADC with independent inputs with each operating at a maximum sampling rate of 1.6 Gsps. When the four single cores are interleaved, it reaches a sample rate of up to 6.4 Gsps [11].

The proposed design would employ under-sampling as the sampling scheme, which makes the band-limiting filter's performance critical in preventing signal aliasing. The basic concepts of aliasing and under-sampling will discussed in the next section, whilst the requirements for the band-limiting filter which has already been derived in [2] and [3] is tabulated in Section 1.3.

1.2.2 Anti-Aliasing Filter Overiew

The theoretical basis for sampling, known as the Nyquist Sampling Theorem, where simply stated, says that the selected sampling frequency must be greater than the highest frequency component of the signal ($\mathrm{f_s} > 2\mathrm{f_{max}}$), else information about the signal will be lost. If this theorem rule is violated, a phenomenon termed "aliasing" will occur [12].

However, the modified version of the Nyquist sampling theorem, called the Nyquist-Shannon Sampling theorem, states that the sampling frequency ($\mathrm{f_s}$) needs to be greater than twice the signal bandwidth (B) and not twice the maximum frequency component ($\mathrm{f_s} > 2\mathrm{B}$), in order to be able to reconstruct the original signal perfectly from the sampled version [13].

The effect of the sampling process in the frequency domain could be conceptualised as a

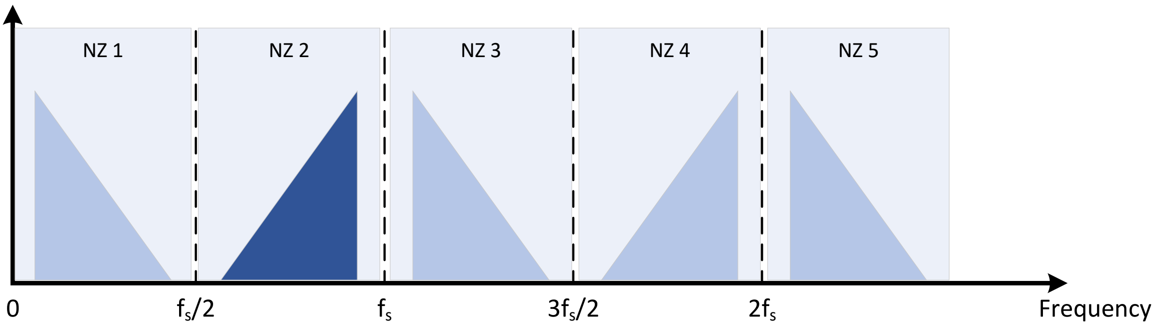

Figure 1.3: Graphical representation of Nyquist zones and spectral inversion [14].

partitioning of regions in the spectrum which are spaced uniformly at intervals of $f_s/2$ [15]. These partitioned regions are referred to as Nyquist zones, denoted as NZ in Figure 1.3. Each of these zones contains either an exact instance of the desired signal, or a mirrored instance thereof. The odd zones (NZ 1, NZ 3, NZ 5. . .) contains the spectral replicas of the desired signal, whereas the even zones (NZ 2, NZ 4. . .) contains the mirrored replicas [14].

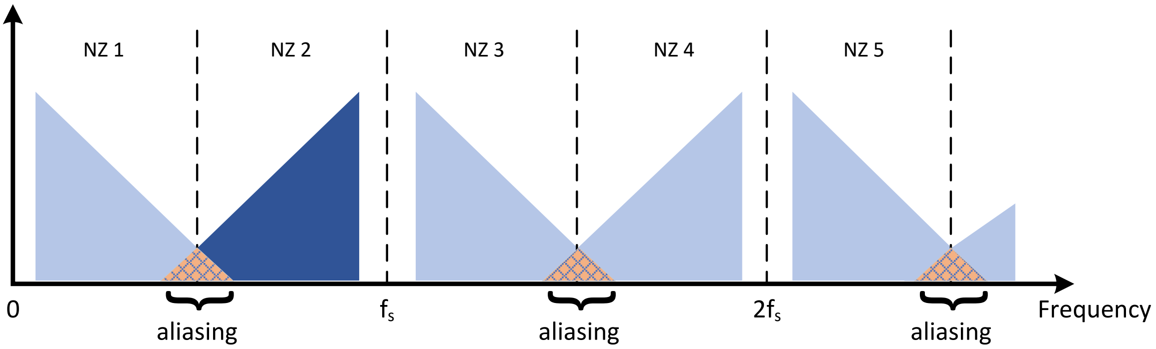

Figure 1.4: Graphical representation of signal aliasing [15].

Aliasing occurs when the bandwidth of the desired signal is greater than half the sampling frequency, resulting in the signal and its replicas to extend beyond the borders of the Nyquist zones, as depicted in Figure 1.4. It is therefore evident that the selection of the sampling frequency needs to be carefully chosen in order to avoid this from occurring.

The next generation digitiser is to employ under-sampling (also known as bandpass sampling) as its sampling technique, which is a process of sampling a signal which lies outside the first Nyquist zone. The sampling frequency for the system has been selected such that the desired signal, having a bandwidth of 2.5 GHz, is symmetrically centred in the middle of the second Nyquist zone at 4.5 GHz, which ensures that the signal and its replicas do not overlap.

In practice, the input signal to the ADC is band-limited by an anti-aliasing filter, which is designed to have a cut-off frequency capable of removing unwanted signals from the ADC input or at least attenuate them enough, such that they do not adversely affect the circuit or cause signal aliasing. Additionally, the stopband of the filter should be as large as possible in order to prevent signal aliasing from other Nyquist zones. Figure 1.5 depicts the required anti-aliasing filter's response suitable for this task.

1.3 Objectives

The goal of this research project is to investigate various suitable planar filter technologies capable of meeting the specifications as outlined in Table 1.1 below. The selected filter is then to be designed, built and tested to validate its performance with respect to these design specifications.

These specifications has already been derived through analysis in [2] and [3] and therefore no further divulgement into the derivation thereof is required. Such analyses is considered to be beyond the scope of this thesis.

Table 1.1: Anti-aliasing Filter Specifications

Parameter	**Specification**
Passband	3.25 GHz - 5.75 GHz
Bandwidth	2.5 GHz
Insertion Loss	≤ 2 dB
Return Loss	≥ 10 dB
Fractional Bandwidth	55.6 %
Stopband attenuation	≥ 23 dB
Lower stopband frequency	2.75 GHz
Upper stopband frequency	6.25 GHz

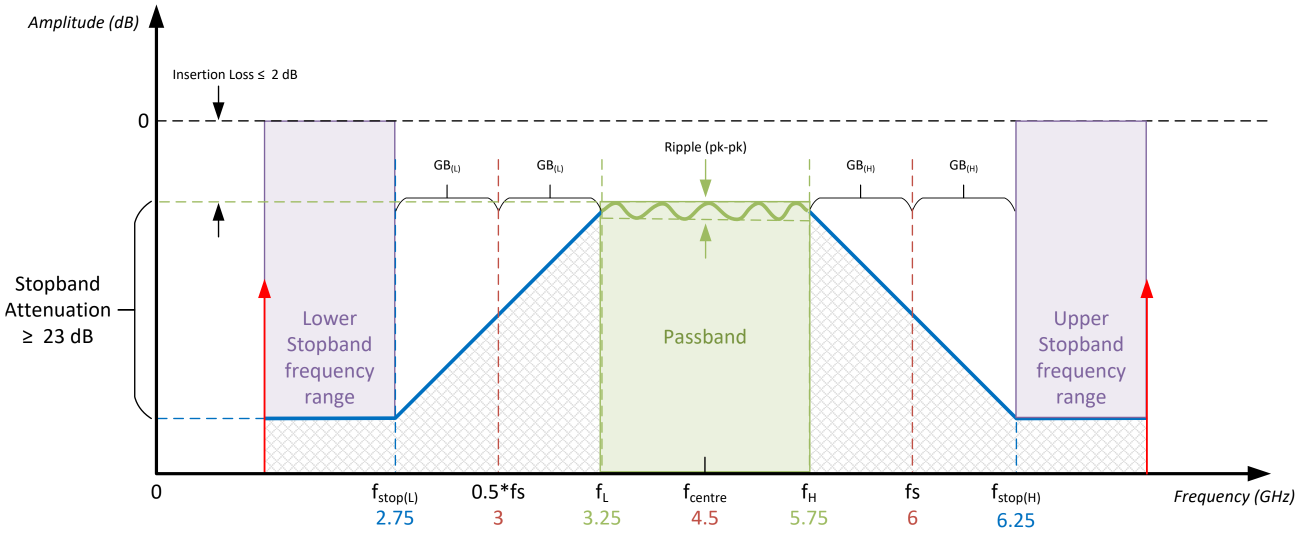

Figure 1.5: Graphical representation of the anti-aliasing filter specifications.

1.4 Document Outline

This thesis is collated with the following structure:

Chapter 2 has the primary purpose of providing some introductory concepts to the design of microwave filters which will be drawn on in the later chapters of this thesis.

Chapter 3 provides an brief overview various wideband planar filter options available which would be suitable in the design of the required anti-aliasing filter.

Chapter 4 details the design steps involved in the development and construction of the selected filter. It furthermore presents the simulated results as well as the measured results.

Chapter 5 presents the conclusions and recommendations.

Chapter 2

Background Theory

This chapter is aimed at providing a basic description of the theories which form the fountain of RF and microwave microstrip filter design. The topics will cover the transfer functions of commonly used filter responses, as well as provide an overview of the insertion loss method to filter design, which includes a brief discussion on the low-pass prototype network, frequency and impedance transformations, impedance and admittance inverters, Richards' transformation, and Kuroda identities for RF and microwave applications where distributed elements are required. A brief overview of microstrip transmission lines will also be addressed.

2.1 Filter Theory Basics

The technical roots of filter theory can be traced back to 1915, where K. Wagner from Imperial Physical Technical Institute (PTR) in Germany and G. Campbell from Bell Laboratories separately invented the electric-wave filter [16].

In subsequent years, the theory was further developed along two distinct methodologies of filter design, i.e. the image parameter method, and the insertion loss method, which is sometimes referred to in literature as classical filter theory and modern filter theory respectively [17]. The image parameter method to filter design involves combining two-port filter sections to achieve the desired cut-off frequencies and is considered to be a relatively simple method. It however has the drawback that an arbitrary frequency response cannot be integrated into the design, which often results in the procedure having to be applied iteratively in order to achieve the desired outcome.

In comparison, the insertion loss method to filter design applies a more systematic and methodical approach to achieving the desired response. The method makes use of network synthesis techniques by using low-pass filter prototypes which have normalised frequencies and impedances, which allows for a relatively high degree of control over the passband characteristics. These prototype networks then undergo transformations which de-normalises the frequency and impedances to the desired range and level.

Most, if not all, modern sophisticated and complex computer-aided design (CAD) packages base their algorithms on the insertion loss method to filter design [18], which removes the burden of performing laborious and lengthy arithmetic calculations using a pocket calculator.

The subsequent sections are aimed at providing only the pertinent concepts and theories required to practical planar filter design. In so doing, an in-depth study on filter network analysis will be omitted from this research, although some of the core concepts may be drawn on where required.

2.1.1 Filter Transfer Functions

The transfer function of a filter is a mathematical representation of a filter network response in the frequency domain, where the input-output filter relationship is described and is generally depicted in a graphical form. This mathematical expression, namely S_{21}, is derived from the two-port circuit network analysis which is common to all RF and microwave filters [19] [20] [21].

The insertion loss method defines the filter response by its insertion loss, or power loss ratio, PLR [14]:

$$P_{LR} = \frac{Power\ available\ from\ source}{Power\ delivered\ to\ load} = \frac{1}{1 - \left|\Gamma\left(\omega\right)\right|^2} \tag{2.1}$$

or in dB:

$$IL = 10 \log P_{LR} \tag{2.2}$$

By network analysis and substitution, the power loss ratio can be rewritten as:

$$P_{LR} = 1 + \frac{M\left(\omega^2\right)}{N\left(\omega^2\right)} \tag{2.3}$$

where M and N are real polynomials in ω^2 and $\Gamma(\omega)$ is the reflection coefficient as a function of ω. The power loss ratio of a physically realisable filter must be in the form of Equation 2.3. The two most commonly used transfer functions used are the Butterworth and Chebyshev functions, which are looked at in the next sub-sections.

2.1.2 Butterworth Response (Maximally Flat)

The Butterworth filter is commonly used in designs that require the amplitude response to be flat as possible, hence it also known as the maximally flat filter. The selectivity of the filter response however compares poorly to the Chebyshev filter response, given the same filter order.

For a Butterworth low-pass filter, its power loss ratio is specified as:

$$P_{LR} = 1 + k^2 \left(\frac{\omega}{\omega_c}\right)^{2n} \tag{2.4}$$

where the ripple constant k relates to a given passband ripple L_{Ar} in dB by:

$$k = \sqrt{10^{\frac{L_{Ar}}{10}} - 1} \tag{2.5}$$

where n is the filter order and ω_c is the cut-off frequency in radians per second. The band edge is defined at the cut-off frequency, where is the power loss ratio (insertion loss) is $1 + k^2$. If at this point, L_{AR} is chosen to be 3 dB, which is the usual case, then $k = 1$. The power loss ratio P_{LR} can then be expressed in dB as:

$$IL = 10 \log \left[1 + \left(\frac{\omega}{\omega_c}\right)^{2n}\right] \tag{2.6}$$

When Equation 2.6 is evaluated at various frequencies for various values of n, a set of curves can be generated, which graphically represents the insertion loss of the filter for various values of n, at various normalised frequencies. This representation is depicted in Figure 2.1.

2.1.3 Chebyshev Response

Chebyshev filters are known for having higher selectivity than the Butterworth filter, especially when the specifications related to the passband ripple is relaxed. This filter response is commonly used in designs that do not require the amplitude response to be flat, allowing ripple to be present in the passband, and when a steeper transition band is required. For a Chebyshev (also known as equal-ripple) low-pass filter, its power loss ratio is specified as:

$$P_{LR} = 1 + k^2 T_n^2 \left(\frac{\omega}{\omega_c}\right) \tag{2.7}$$

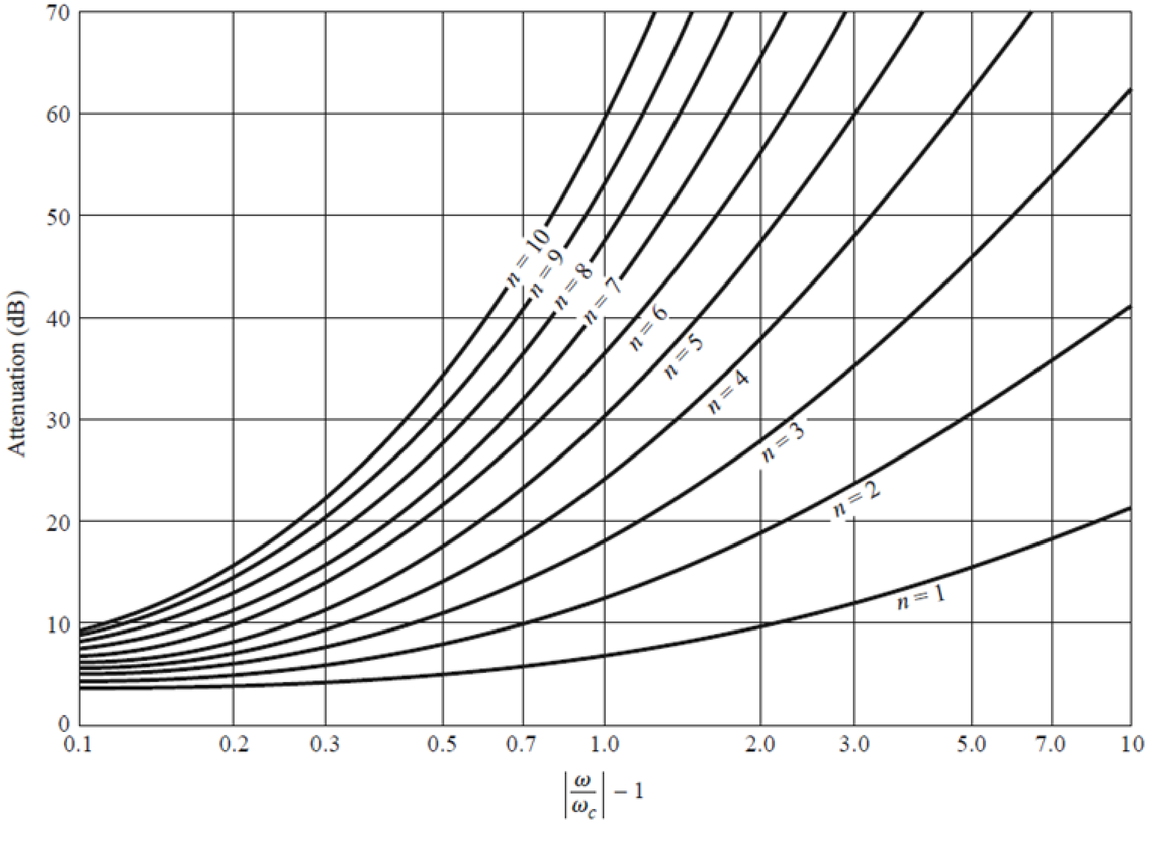

Figure 2.1: Butterworth attenuation curves for various values of n [18].

where the ripple constant k relates to a given passband ripple L_{Ar} in dB by:

$$k = \sqrt{10^{\frac{L_{Ar}}{10}} - 1} \tag{2.8}$$

and $T_n(x)$ is the Chebyshev polynomial of the first kind with a degree of n. When letting $x = \cos\theta$ for $|x| < 1$, then Chebyshev polynomial can be generally expressed as [18]:

$$T_n(x) = \begin{cases} \cos(n\cos^{-1}x) & |x| < 1 \\ \cosh(n\cosh^{-1}x) & x > 1 \end{cases} \tag{2.9}$$

Figures 2.2 and 2.3 depict graphically the evaluation of Equation 2.9 for passband ripple levels of 0.5 dB and 3 dB for various values of n, at various normalised frequencies.

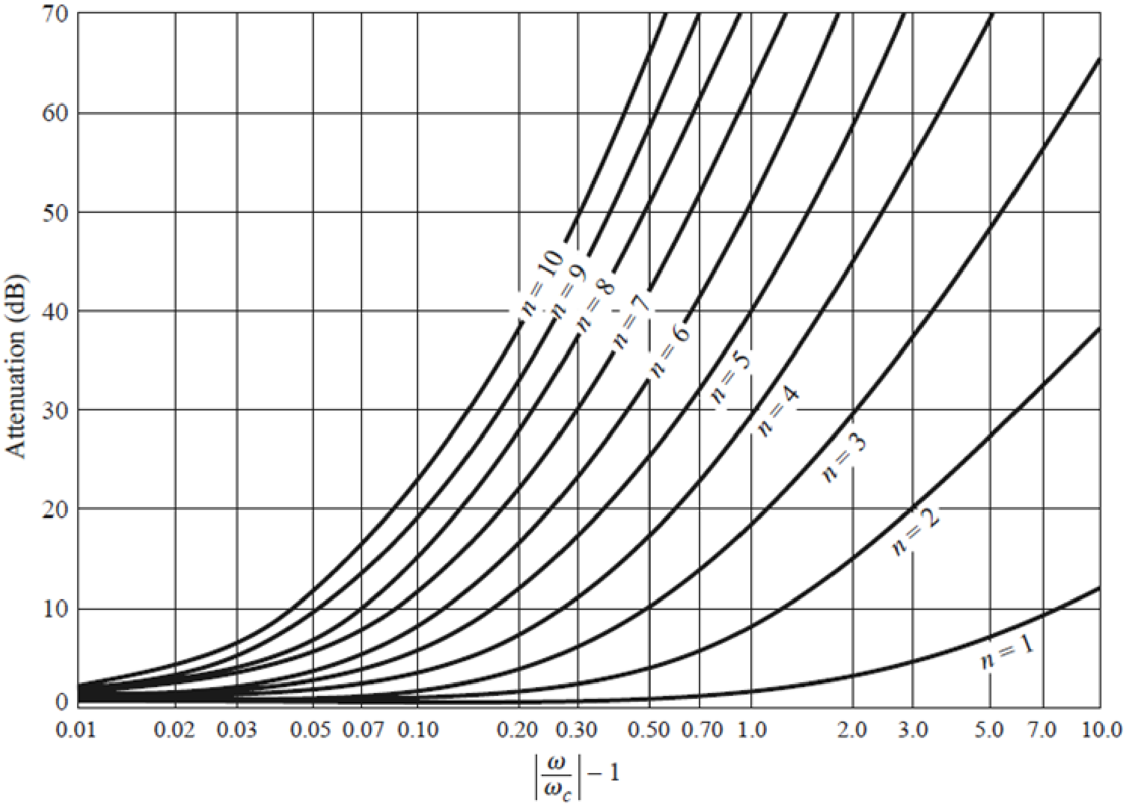

Figure 2.2: Chebyshev filter response with 0.5 dB ripple level [18].

2.1.4 Insertion Loss Method to Filter Design

Although both the image parameter method and insertion loss method to filter design yields practical circuits using lumped elements, the discussion will only consider the latter method since most modern design tool CAD packages are based on this method. Figure 2.4 below broadly outlines the steps involved to filter design using this method [18]. The fundamental concept of the insertion loss method is to find the closed-form transfer function that can accurately present the frequency response of a filter [22]. For applications at microwave frequencies, the filter design is transformed from lumped elements to distributed elements made up of transmission line sections due to the limitations and losses associated with lumped elements at these frequencies. This will be addressed in the “implementation” stage of the design process.

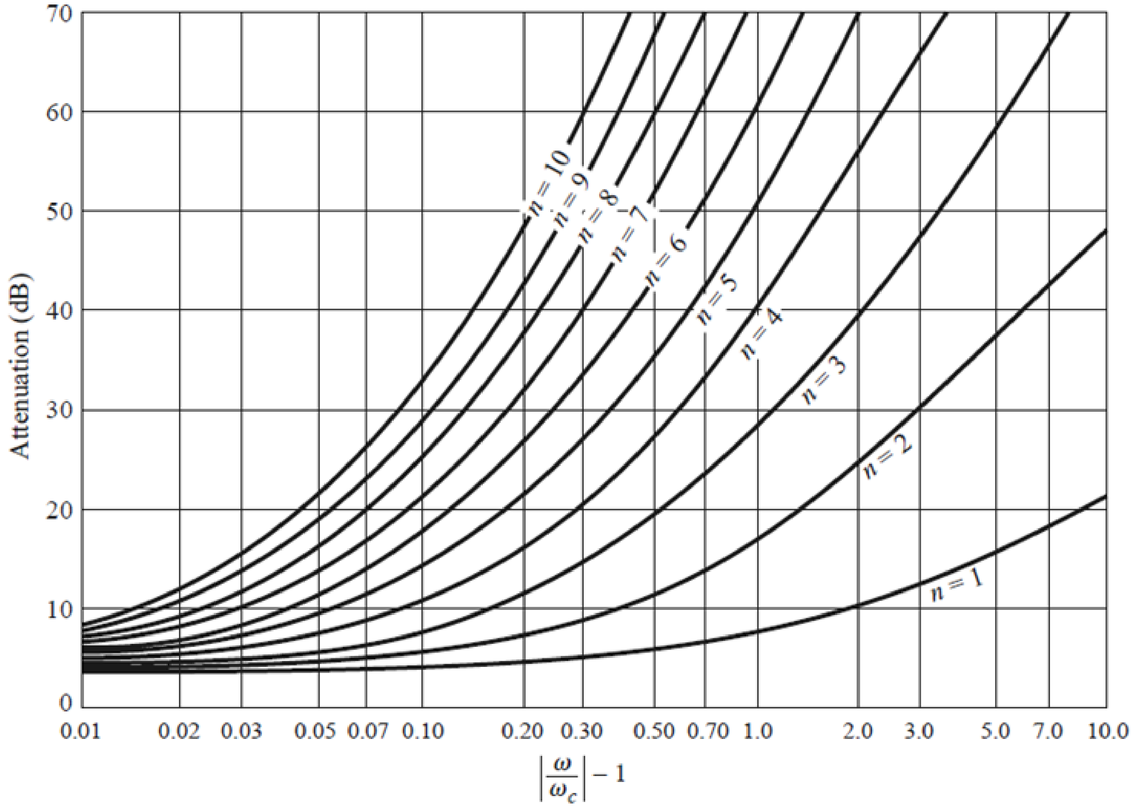

Figure 2.3: Chebyshev filter response with 3 dB ripple level [18].

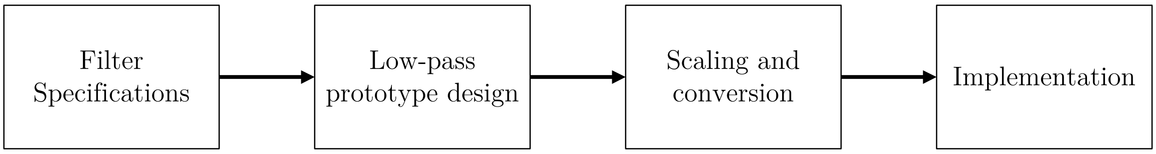

Figure 2.4: Design flow of insertion loss method [18].

2.1.5 Low-Pass Prototype Design

The analytical approach to filter design by using the insertion loss method allows a "catalogue" of useful and practical filter circuits to be tabulated for ease of reference. The concept of normalisation is central to cataloguing since it allows filter designers to comparatively evaluate different filter types given the same operating criteria [23]. The low-pass prototype circuit consists of a network of cascaded series and shunt elements, where the element values are normalized such that the source impedance is 1 Ω and the cut-off frequency $\omega_c = 1$ radian per second, depicted in Figure 2.5 and its dual in Figure 2.6.

The element values are sequentially numbered from the generator impedance g_0, to the load

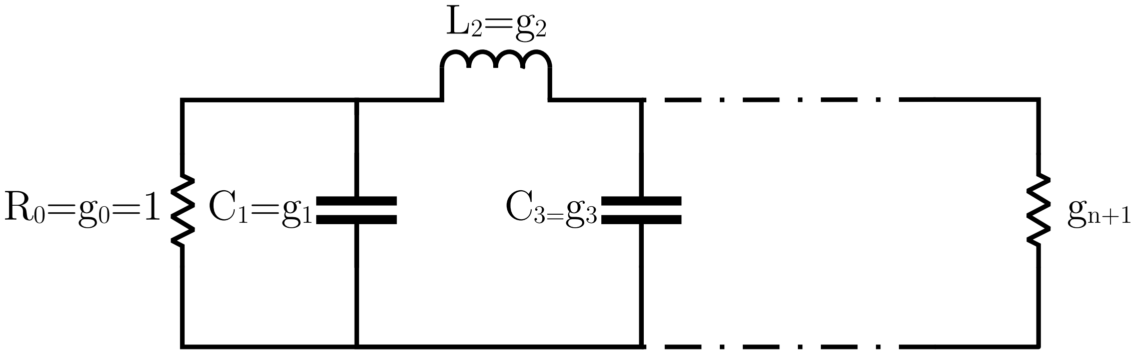

Figure 2.5: Low-pass prototype circuit with shunt element first [18].

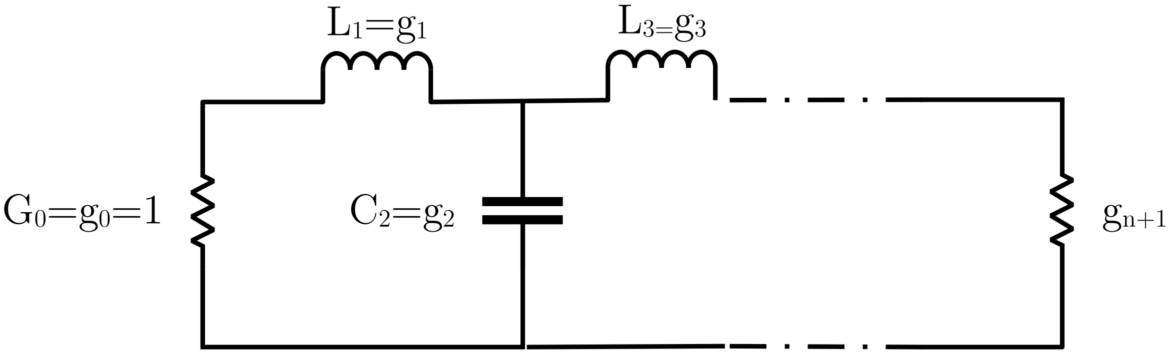

Figure 2.6: Low-pass prototype circuit with series element first [18].

impedance numbered as g_{n+1}. The number of reactive elements in the network denoted by n, indicates the degree or order of the filter. The element values can be determined by using various filter synthesis procedures [22], or they can be computed by using the following closed-form expressions [18] for commonly used low-pass prototype filters:

For the Butterworth low-pass prototype filter:

$$\begin{aligned} \mathrm{g}_0 &= 1 \\ \mathrm{g}_k &= 2\sin\left[\frac{(2k-1)\,\pi}{2n}\right] \quad ,k = 1,\ 2,\ ...,\ n \\ \mathrm{g}_{n+1} &= 1 \end{aligned} \tag{2.10}$$

For the Chebyshev (equal-ripple) low-pass prototype filter:

$$\begin{aligned} \mathrm{g}_1 &= \frac{2a_1}{\sinh\left(\frac{\beta}{2n}\right)} & & \\ \mathrm{g}_k &= \frac{4a_{k-1}a_k}{b_{k-1}\mathrm{g}_{k-1}} & &, k = 2,\ 3,\ ..., n \\ \mathrm{g}_{n+1} &= 1 & & \text{for } n \text{ odd} \\ \mathrm{g}_{n+1} &= \coth^2\left(\frac{\beta}{4}\right) & & \text{for } n \text{ even} \end{aligned} \tag{2.11}$$

where

$$\begin{aligned} \beta &= \ln\left(\coth\frac{L_{Ar}}{17.37}\right) & & \\ a_k &= \sin\left[\frac{(2k-1)\,\pi}{2n}\right] & &, k = 1,\ 2,\ ...,\ n \\ b_k &= sinh^2\left(\frac{\beta}{2n}\right) + sin^2\left(\frac{k\pi}{n}\right) & &, k = 1,\ 2,\ ...,\ n \end{aligned} \tag{2.12}$$

For convenience, [21] tabulates the Butterworth and Chebyshev (equal-ripple) low-pass prototype filter element values for the various passband ripples L_{Ar}, and values of n from 1 to 15. The g values, unless otherwise specified, are either inductance (H), capacitance (F), resistance (Ω), or conductance ($\mho$).

In practical filter design, the minimum stopband attenuation L_{As} at frequency Ω_s is usually dictated by the given specification, where the required low-pass prototype filter order, n, can be interpolated from Figures 2.1 – 2.3 or can approximated by Equation 2.13 for a Butterworth response and Equation 2.14 for a Chebyshev (equal-ripple) response [19].

$$n \ \geq \ \frac{\log\left(10^{0.1L_{As}} - 1\right)}{2\log\Omega_s} \tag{2.13}$$

$$n \geq \frac{\cosh^{-1}\sqrt{\frac{10^{0.1L_{As}-1}}{10^{0.1L_{Ar}-1}}}}{\cosh^{-1}\Omega_s} \tag{2.14}$$

$$\Omega_s = \frac{f_s}{f_c} \tag{2.15}$$

where the specified filter stopband frequency is denoted by f_s and the filter cut-off frequency is denoted by f_c.

2.1.6 Scaling and Conversion

Since the low-pass filter prototype circuits discussed in the previous sections are normalised having source impedance of $Rs = 1\ \Omega$ and a cut-off frequency of $\omega_c = 1$ radian per second, it is now necessary to de-normalise them in order to create a practical filter circuit.

Impedance Scaling:

In the case where g_0 denotes the generator resistance R_0 (Figure 2.6), the impedance scaling can be achieved by multiplying all the impedances of the low-pass prototype circuit by R_0. The scaled filter element values given by

$$\begin{aligned} L' =&\ R_0 L \\ C' =&\ \frac{C}{R_0} \\ {R_s}' =&\ R_0 \\ {R_L}' =&\ R_0 R_L \end{aligned} \tag{2.16}$$

where the primed values denote the scaled quantities and L, C and R_L are the element values of the prototype circuit.

Frequency Scaling:

The transformation of the cut-off frequency for a low-pass prototype circuit from unity to ω_c is done by scaling the frequency dependence of the filter by the factor $\frac{1}{\omega_c}$, which can be achieved by replacing ω by $\frac{\omega}{\omega_c}$ [18]. The frequency scaled element values denoted by prime, are determined by

$$\begin{aligned} {L_k}' =&\ \frac{L_k}{\omega_c} \\ {C_k}' =&\ \frac{C_k}{\omega_c} \end{aligned} \tag{2.17}$$

When scaling both the impedance and frequency, Equations 2.16 and 2.17 can be combined to give

$$\begin{aligned} {L_k}' &= \frac{R_0 L_k}{\omega_c} \\ {C_k}' &= \frac{C_k}{R_0 \omega_c} \end{aligned} \tag{2.18}$$

<u>Conversion:</u>
Filter prototype circuit transformations from low-pass to high-pass, band-pass, or band-stop can be achieved by replacing the frequency dependent variable with the appropriate scaling factor, as well as transforming the series and shunt elements to components or resonant circuits. A summary [18] of these transformations is depicted in Figure 2.7.

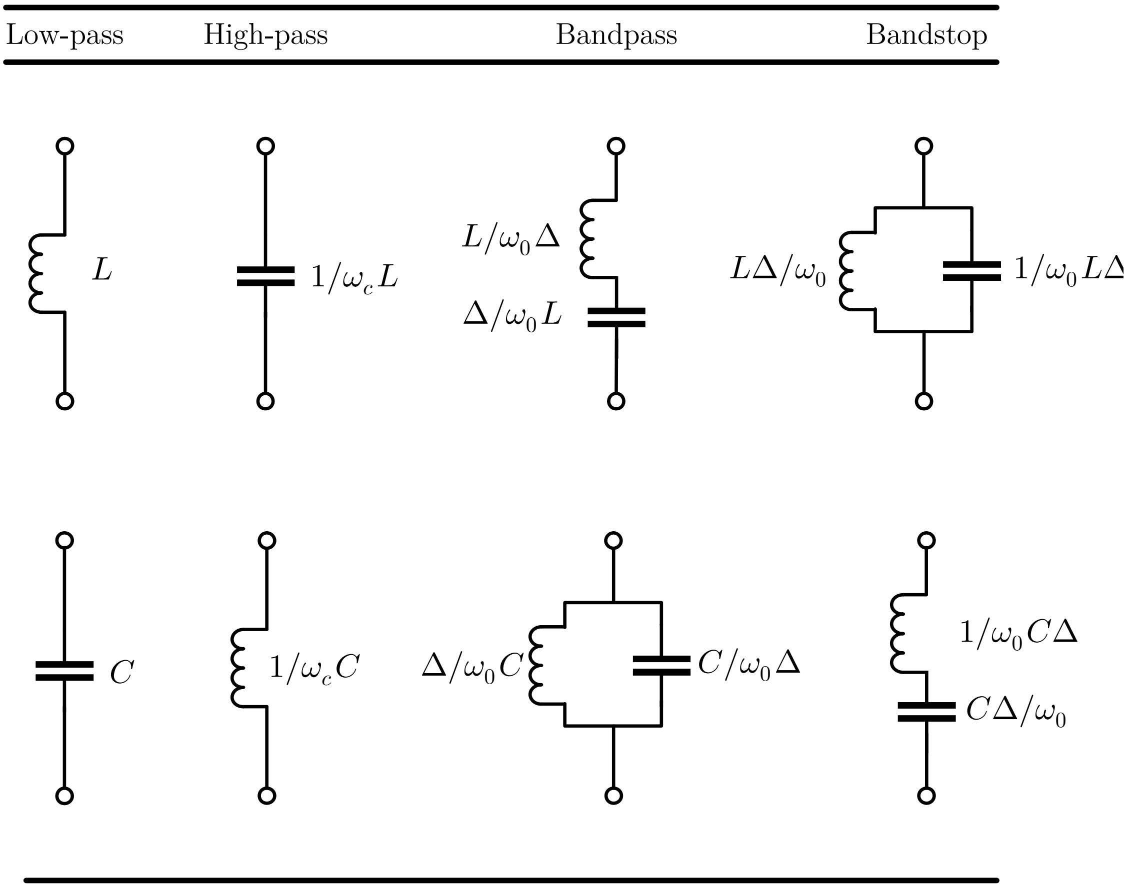

Figure 2.7: Prototype filter transformations summary.

with

$$\begin{aligned} \Delta &= \frac{\omega_2 - \omega_1}{\omega_0} \\ \omega_0 &= \sqrt{\omega_1 \omega_2} \end{aligned} \tag{2.19}$$

where Δ is the fractional bandwidth (FBW) and ω_0 is the center frequency.

2.1.7 Implementation

At higher RF and microwave frequencies, the use of lumped components becomes unusable to implement in terms of size, and are generally only available for a very limited range of values [18]. Furthermore, at these higher frequencies the parasitic effects become more significant, where the increasing frequency results in higher losses and spurious resonances. Additionally, lumped element components exhibits a lower Q-factor when compared to distributed elements [24].

To overcome this, distributed elements in the form of transmission line sections are used to approximate lumped components. A brief overview of the processes required to achieve this transformation will be addressed next.

Richard's transform:

In order to convert lumped elements to distributed transmission line sections, a process called Richard's Transform is used [18]. The fundamental concept of this transformation focuses on making use of open- and short-circuited transmission line stubs to represent a lumped capacitor or inductor. The transformation given by Equation 2.20 maps the frequency plane (ω) to the complex plane (Ω), which repeats every $\frac{\omega l}{vp} = 2\pi$.

$$\Omega = \tan \beta l = \tan \left(\frac{\omega l}{v_p} \right) \tag{2.20}$$

where $\frac{\omega l}{v_p}$ is the ratio of a length of the basic commensurate transmission-line element to the phase velocity of the wave in such a line element, and β is phase constant.

By replacing the frequency variable ω with the complex variable Ω, the reactive inductance and the capacitive susceptibility can be rewritten as follows

$$\begin{aligned} jX_L &= j\omega L = j\Omega L = jL \tan \beta l \\ jX_C &= j\omega C = j\Omega C = jC \tan \beta l \end{aligned} \tag{2.21}$$

Under Richards' transformation, a close correspondence exists between lumped inductors and capacitors in the frequency plane (ω) and short- and open-circuited transmission lines in the complex plane (Ω) [19].

This shown by Equation 2.21 where a lumped-element inductor can be replaced with a short-circuited transmission line of length βl with a characteristic impedance of L, whilst a lumped-element capacitor can be replaced with a open-circuited transmission line of length βl with a characteristic impedance of $\frac{1}{C}$, as depicted in Figure 2.8.

For a low-pass filter prototype filter with unity impedance, the cut-off occurs at the unity frequency. Therefore, Equation 2.20 can now be expressed as $\Omega = \tan \beta l = 1$ which equates to a stub length of $\frac{\lambda}{8}$ at the cut-off frequency ω_c. Due to the stubs all having the same electrical length at ω_c, they are also termed as commensurate lines.

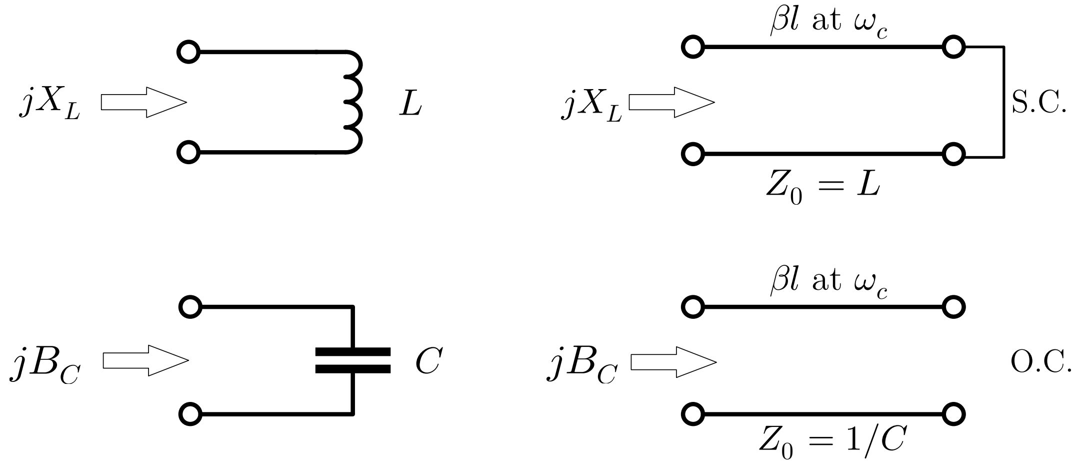

Figure 2.8: Richards' transformation for lumped elements to distributed transmission lines.

Kuroda identities:

The four Kuroda identities are very useful transforms that uses of commensurate-length lines to convert the implementation of Richard's Transform to a more suitable form for physical realisation whilst maintaining its electrical equivalence.

The four Kuroda identities is depicted in Figure 2.9, where $n^2 = 1 + \frac{Z_2}{Z_1}$, can be used to:

- Physically separate transmission line stubs with the addition of unit elements
- Transform transmission line stubs from series to shunt, or vice versa
- Change impractical characteristic impedances into values which are more physically realisable

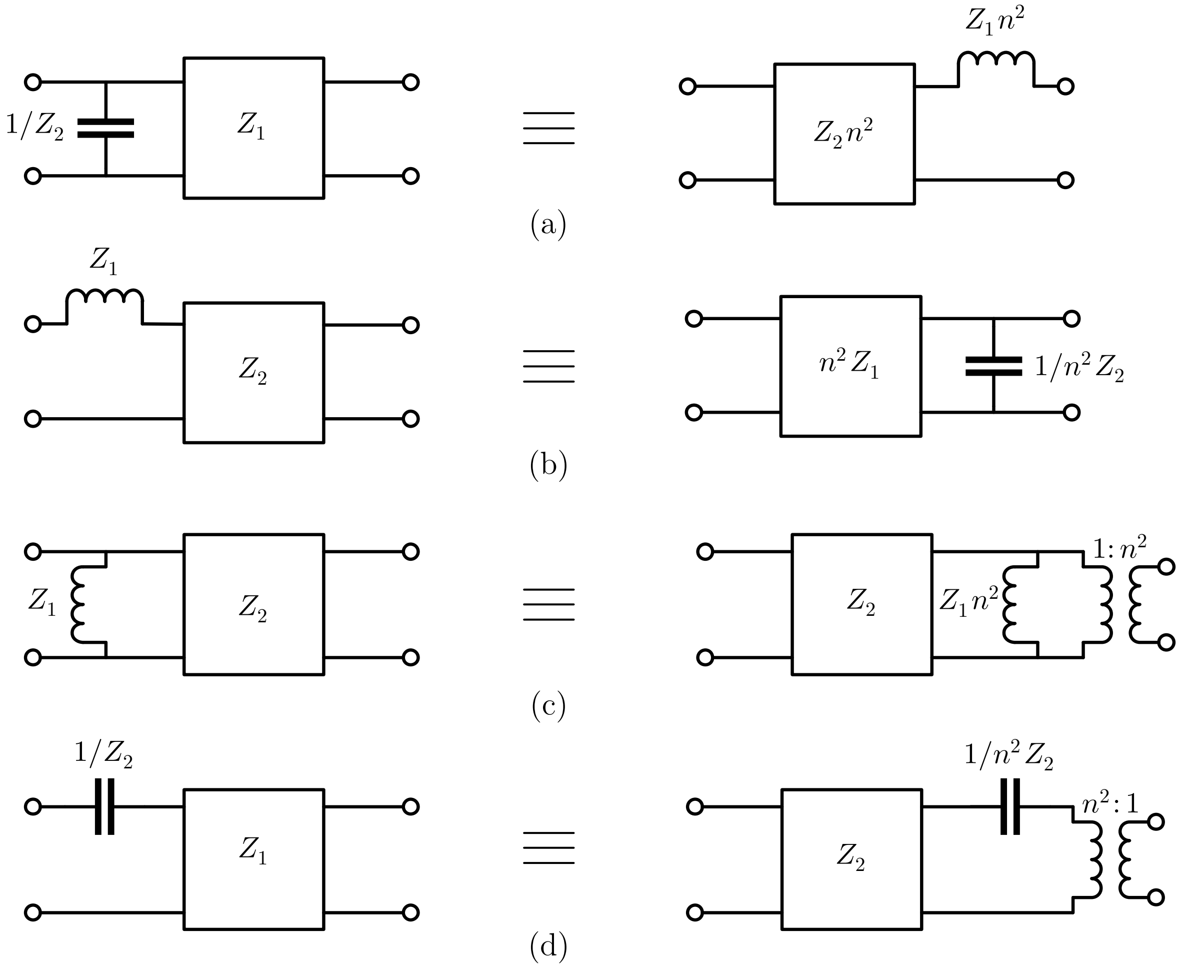

Figure 2.9: The Kuroda Identities.

2.1.8 Immitance Inverters (J-K Inverters)

Impedance and Admittance Inverters is an alternative element conversion method to the Kuroda Identities, where it can also be used to transform series-elements to shunt-elements, and vice versa, in order to make the implementation of a filter circuit more realisable, particularly in the case of band-pass and band-stop filter circuits.

The theoretical operation of the impedance inverter hinges on the notion that they essentially form the inverse of the load impedance or admittance as depicted in Figure 2.10(a), thereby allowing series-elements to be transformed to shunt-element, and vice versa.

In its most basic form, these inverters can be represented by a quarter-wave transformer of the appropriate characteristic impedance [18] as depicted in Figure 2.10(b).

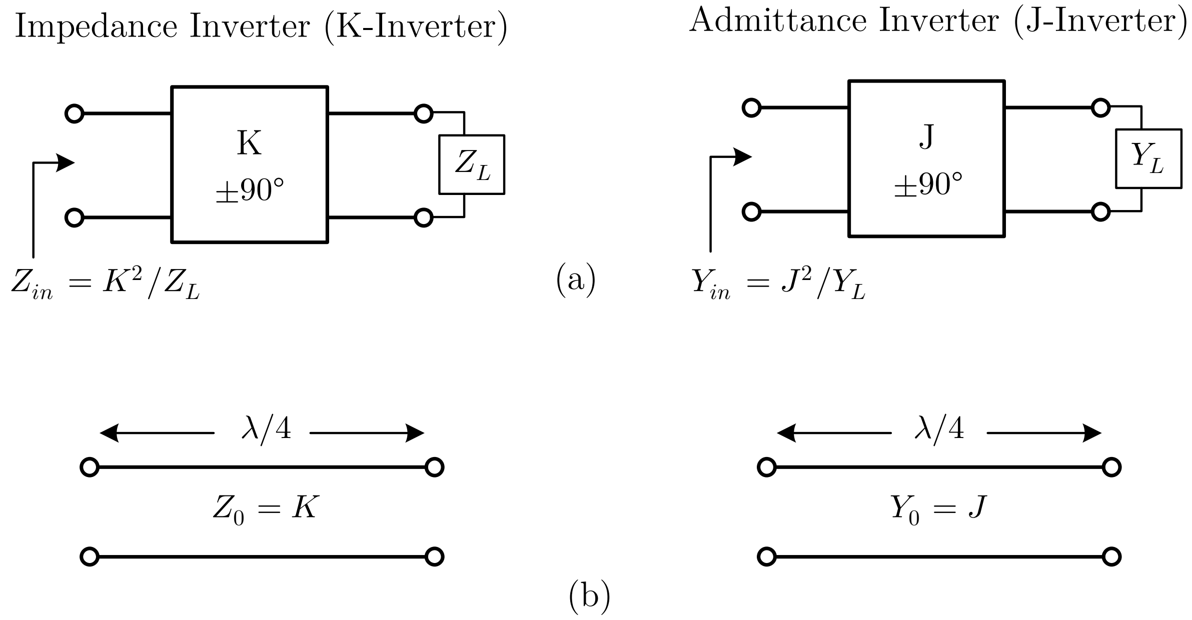

Figure 2.10: Impedance and admittance inverters.

2.2 Microstrip Transmission Line Basics

The microstrip transmission line is one the most commonly used planar structures due to its ease of manufacturing through photolithographic techniques, as well as the ease of integration with active and passive devices. Its form, depicted in Figure 2.11 [19], consists of a conductor of width W, which is constructed on a thin grounded substrate of thickness h with a relative permittivity ϵ_r. The electromagnetic (EM) field distribution extend within the two media, namely the air above the conducting strip and the dielectric below it, thereby making the structure inhomogeneous to the propagating EM waves as shown in Figure 2.12 [18].

The inhomogeneous nature of the microstrip structure means it does not support a pure TEM wave due to the difference in phase velocity through the two mediums. This difference makes it impossible to enforce a phase-matching condition at the interface between the mediums.

In reality, the fields of a microstrip line contains a so-called hybrid mode, consisting of a TM-TE wave. In practice, the realised structure has an electrically very thin dielectric substrate, which allows the longitudinal EM field component for the dominant mode to remain much smaller than the transversal EM field component, which means it may be neglected and thereby allowing the dominant mode to behave similar to a TEM mode. This is called the quasi-TEM approximation, which is supported by microstrip [18].

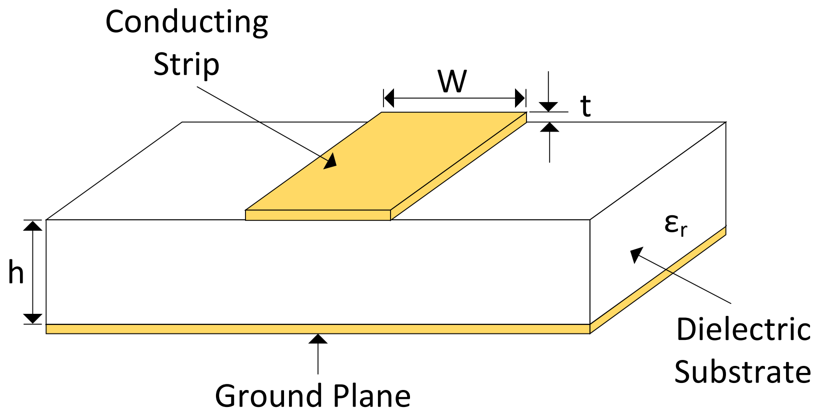

Figure 2.11: Microstrip geometry [19].

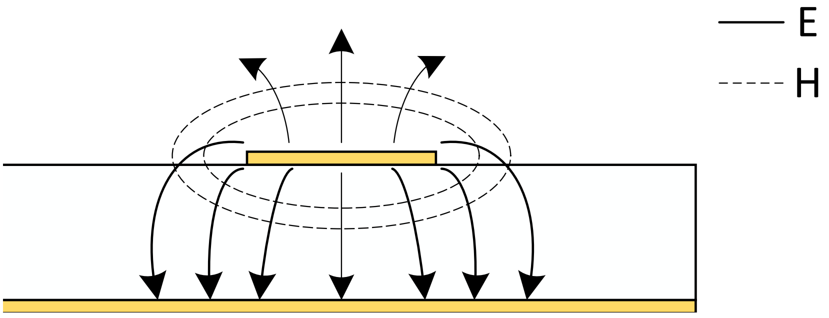

Figure 2.12: Microstrip EM distribution [18].

2.2.1 Effective Dielectric Constant and Characteristic Impedance

Transmission characteristics of a microstrip structure are primarily described by the effective dielectric constant, denoted as ϵ_e, and characteristic impedance, denoted as Z_0, which can be obtained by quasi-static analysis, where the effective dielectric constant is determined by the approximation [18][19]:

For $\frac{W}{h} \geq 1$:

$$\epsilon_e = \frac{\epsilon_r + 1}{2} + \frac{\epsilon_r - 1}{2} \frac{1}{\sqrt{1 + 12h/W}} \tag{2.22}$$

For $\frac{W}{h} \leq 1$:

$$\epsilon_e = \frac{\epsilon_r + 1}{2} + \frac{\epsilon_r - 1}{2} \left\{ \frac{1}{\sqrt{1 + 12h/W}} + 0.04 \left[1 - (\frac{W}{h})^2 \right] \right\} \tag{2.23}$$

The characteristic impedance given the dimensions of a microstrip line can be determined as:

For $\frac{W}{h} \geq 1$:

$$Z_0 = \frac{60}{\sqrt{\epsilon_e}} \ln\left(\frac{8h}{W} + \frac{W}{4h}\right) \tag{2.24}$$

For $\frac{W}{h} \leq 1$:

$$Z_0 = \frac{120\pi}{\sqrt{\epsilon_e}\left[W/h + 1.393 + 0.667\ln\left(W/h + 1.444\right)\right]} \tag{2.25}$$

For a given characteristic impedance Z_0 and substrate relative permittivity ϵ_r, the $\frac{W}{h}$ ratio can be determined by using the synthesis equations derived by Wheeler [25] [26] and later revised by Hammerstad [27], given as:

For $\frac{W}{h} \leq 2$:

$$\frac{W}{h} = \frac{8e^{A}}{e^{2A} - 2} \tag{2.26}$$

with

$$A = \frac{Z_0}{60}\sqrt{\frac{\epsilon_r + 1}{2}} + \frac{\epsilon_r - 1}{\epsilon_r + 1}\left(0.23 + \frac{0.11}{\epsilon_r}\right) \tag{2.27}$$

For $\frac{W}{h} \geq 2$:

$$\frac{W}{h} = \frac{2}{\pi}\left\{(B - 1) - ln\left(2B - 1\right) + \frac{\epsilon_r - 1}{2\epsilon_r}\left[ln\left(B - 1\right) + 0.39 - \frac{0.61}{\epsilon_r}\right]\right\} \tag{2.28}$$

with

$$B = \frac{377\pi}{2Z_0\sqrt{\epsilon_r}} \tag{2.29}$$

Chapter 3

Planar Filter Technologies

Microwave filter design has come a long way since the 1950's [18]. As years pass and newer technologies emerge, more and more researchers and designers continue to find innovative ways of improving on some of the fundamental microwave filter design techniques as described in [21]. The selection of which microwave filter technology to use is largely influenced by two key specifications, namely the filter's operating frequency and the filter bandwidth or fractional bandwidth.

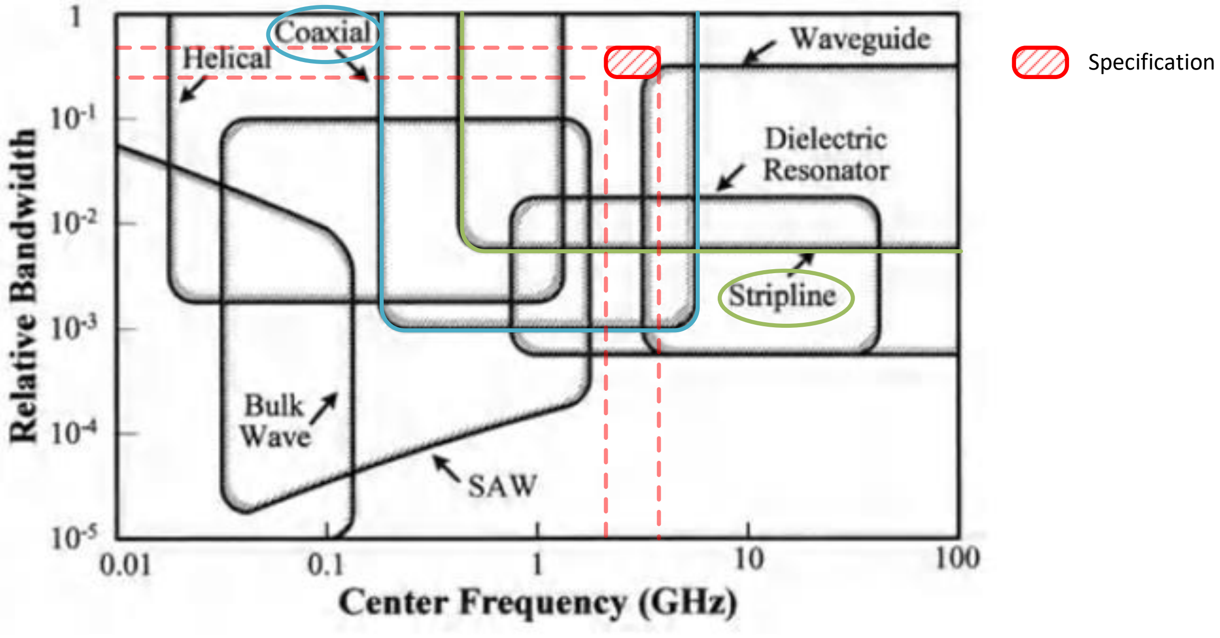

Figure 3.1: Common Filter Technologies [28].

Figure 3.1 depicts filter technologies which are commonly used at low frequencies as well as at RF and microwave frequencies. It additionally depicts an overlaid area of the specifications for the required filter in order to gain a better overview. Based on this, the most suited filter technologies able to meet the required anti-aliasing bandpass filter specifications are coaxial, stripline and microstrip filters.

Coaxial resonator filters presents many attractive features such as low-loss, and has virtually no radiation losses which is attributed to it's metallic enclosure. It does however have the disadvantage of being larger in circuit size and relatively hard to integrate with other circuits when compared to stripline or microstrip filter technologies. Other attributes that places this technology at a disadvantage to stripline and microstrip filters are tabulated in Table 3.1 [18].

Table 3.1: Filter technology comparison

Characteristic	**Coaxial**	**Stripline**	**Microstrip**
Dispersion	None	None	Low
Bandwidth	High	High	High
Loss	Medium	High	High
Power Capacity	Medium	Low	Low
Physical Size	Large	Medium	Small
Ease Of Fabrication	Medium	Easy	Easy
Circuit Integration	Hard	Fair	Easy

When considering of all these factors, it becomes clear that stripline and microstrip technology would be the best suited filter technology for the required anti-aliasing bandpass filter due to the added benefit of being smaller in size and ease of integration.

The fundamental and conventional filter theory discussed in Chapter 2 is based on narrow-to-moderate bandwidth filter designs. This presents somewhat of a challenge since the required anti-aliasing filter is specified to have fractional bandwidth of 55.6%. This wide bandwidth specification classes the required filter in the category of ultra-wideband (UWB) filters, where in some instances the previously discussed theories cannot be directly applied to the design of UWB bandpass filters [29]. The discussed filter implementations in this chapter will explore some of the novel design techniques which were specifically developed by researchers and filters designers for use in UWB applications. The required filter however does not have to conform to the regulations surrounding UWB filters such as emission levels, and neither has to achieve the full specified FBW of 109.5%, and therefore will only look at the techniques used to achieve a wider bandpass response.

A vast array of novel and innovative techniques related to UWB bandpass filter designs are being regularly reported in various literature sources [30][31][32][33][34]. Some of these reported techniques are complex in design and prove to be expensive to manufacture. Others are low in complexity but suffer from large circuitry sizes. Several suitable planar UWB design techniques will be addressed in this chapter, more specifically designs where microstrip implementations are utilised due to its ease of circuit integration with other discrete and active components, as well as having lesser manufacturing costs when compared to that of stripline.

3.1 Overview of Ultra-wideband (UWB) Technology

3.1.1 Technology

The terminology “Ultra-wideband (UWB)“, which commonly refers to signals with a large relative bandwidth, was first used by the Defense Advanced Research Projects Agency (DARPA) in 1989 [35], where its application was solely authorized for Military. Since the announcement of the U.S Federal Communications Commission (FCC) in February 2002 releasing the UWB spectrum for commercial use, the development of the technology have become a sought after research topic and has subsequently undergone significant changes and advancements due to it’s attractiveness.

3.1.2 Definition and Bandwidth

According to [36], the specified operational frequency band for communication and measurement systems ranges from 3.1 GHz to 10.6 GHz, which warrants an unprecedented bandwidth of 7.5 GHz. Furthermore it is specified that the -10 dB fractional bandwidth (FBW) of an UWB signal be greater than 20% or have a minimum -10 dB bandwidth of 500 MHz. The proposed equation(s) for calculating the FBW and centre frequency of an UWB signal is given as:

$$FBW = 2\left(\frac{f_H - f_L}{f_H + f_L}\right) \tag{3.1}$$

$$f_0 = \frac{(f_H + f_L)}{2} \tag{3.2}$$

where:
FBW is the -10 dB fractional bandwidth,
f_H is the upper frequency of the -10 dB emission point,

f_L is the lower frequency of the -10 dB emission point, and
f_0 is the centre frequency of the UWB signal.

For the specified UWB operational frequency band, it equates to a FBW of 109.5% and a centre frequency of 6.85 GHz.

3.2 Quarter-Wave Shunt Short-Circuited Stubs

The microstrip filter design technique which employs the quarter wavelength short-circuited stub is widely reported in literature due to its many attractive features. It is able to achieve moderate to wide bandwidths by simply increasing the order of the filter whist maintaining a reasonably compact size. It is also cheap to manufacture, due the photolithographic techniques used in producing microstrip, and relatively easy to integrate with other circuitry [18].

This filter can be designed using the conventional filter theory discussed in Chapter 2. As mentioned, the insertion loss filter design method uses network synthesis techniques, and begins with a low pass filter prototype that has normalised impedance and frequency elements. It is then transformed to the required filter response, namely high-pass, bandpass or bandstop by using the design equations described in Chapter 2 and [21].

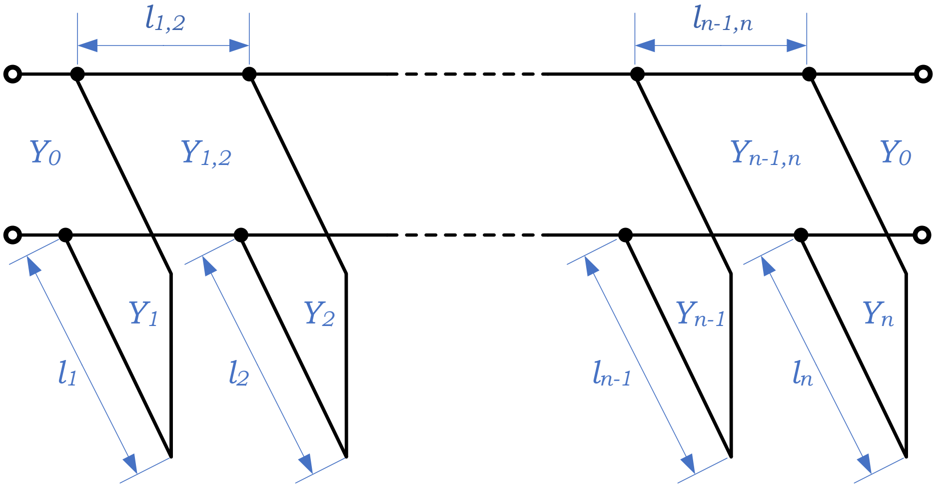

Figure 3.2: Transmission line bandpass filter with quarter-wavelength short-circuited stubs.

The transformed theoretical filter prototype is then further transformed to have the form depicted in Figure 3.2 by using the following set of design equations for a given filter degree n [19]:

$$
\begin{aligned}
\theta &= \frac{\pi}{2}\left(1-\frac{FBW}{2}\right) \\
h &= \ 2 \\
\frac{J_{1,2}}{Y_0} &= \mathrm{g}_0\sqrt{\frac{h\mathrm{g}_1}{\mathrm{g}_2}} \\
\frac{J_{n-1,n}}{Y_0} &= g_0\sqrt{\frac{h\mathrm{g}_1\mathrm{g}_{n+1}}{\mathrm{g}_0\mathrm{g}_{n-1}}} \\
\frac{J_{i,i+1}}{Y_0} &= \frac{h\mathrm{g}_0\mathrm{g}_1}{\sqrt{\mathrm{g}_i\mathrm{g}_{i+1}}} && \text{for } i = 2 \text{ to } n-2 \\
N_{i,i+1} &= \sqrt{\left(\frac{J_{i,i+1}}{Y_0}\right)^2 + \left(\frac{h\mathrm{g}_0\mathrm{g}_1 tan\theta}{2}\right)^2} && \text{for } i = 1 \text{ to } n-1 \\
Y_1 &= \mathrm{g}_0 Y_0\left(1-\frac{h}{2}\right)\mathrm{g}_1 tan\theta + Y_0\left(N_{1,2}-\frac{J_{1,2}}{Y_0}\right) \\
Y_n &= Y_0\left(\mathrm{g}_n\mathrm{g}_{n+1}-\mathrm{g}_0\mathrm{g}_1\frac{h}{2}\right) tan\theta + Y_0\left(N_{n-1,n}-\frac{J_{n-1,n}}{Y_0}\right) \\
Y_i &= Y_0\left(N_{i-1,i}+N_{i,i+1}-\frac{J_{i-1,i}}{Y_0}-\frac{J_{i,i+1}}{Y_0}\right) && \text{for } i = 2 \text{ to } n-1 \\
Y_{i,i+1} &= Y_0\left(\frac{J_{i,i+1}}{Y_0}\right) && \text{for } i = 1 \text{ to } n-1
\end{aligned}
\tag{3.3}
$$

where h is a dimensionless constant, which could be assigned another value in order to achieve a convenient admittance level in the interior of the filter. The physical length l of the stubs and connecting lines are determined by the electrical length θ and the associated propagation constant β as follows:

$$\beta = \frac{2\pi}{\lambda_g} \tag{3.4}$$

$$\theta = \beta l \tag{3.5}$$

The length of stubs and connecting lines are all $\frac{\lambda_g}{4}$ long, which equates to an electrical length of $\frac{\pi}{2}$ radians or 90°. The microstrip line widths can then be determined by using the synthesis Equations 2.26 or 2.28 for a given substrate. The quarter-wave shunt short-circuited bandpass design was used in [3] where an 8^{th} order Chebyshev filter centred at 4.5 GHz was designed and built. The short-circuited stubs have been staggered to limit the coupling between the stubs which could cause spurious responses out of band as depicted in Figure 3.3.

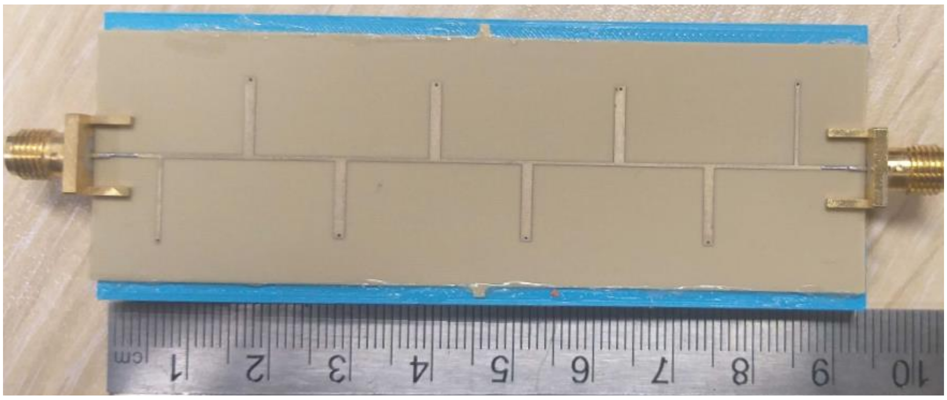

Figure 3.3: Fabricated quarter-wave shunt short circuited bandpass filter from [3].

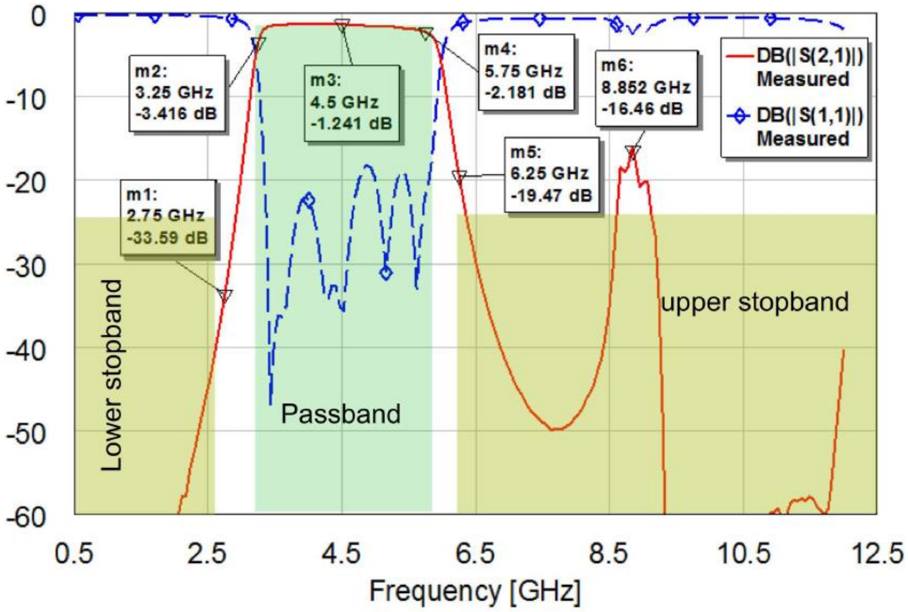

Figure 3.4: Measured performance of the bandpass filter from [3].

The filter performance does not entirely meet the specification, but achieves good correlation between the simulated and measured results. The filter met the specified fractional bandwidth of 55.6% and return loss of more than 10 dB over the passband, but failed to meet the upper stopband rejection specification of 23 dB at 6.25 GHz. From Figure 3.4, the filter seems to have a second passband centred at $3\omega 0$ and also exhibits an attenuation pole at $2\omega 0$, which is a typical stopband characteristics of this type of filter topology [19].

One commonly used method to improve on this inherent out-of-band characteristic is to cascade it with a low-pass filter, but will unfortunately add to the overall circuit size. A discussion relating to cascased filter circuits will be adressed in the next section.

3.3 Cascaded High-pass Low-pass Filters

Arguably the most simple and intuitive way of designing a wideband bandpass filter is to cascade a high-pass filter with a low-pass filter [22]. A simple conceptual view of the outcome of this is depicted in Figure 3.5. Cascading them presents the advantage of having an overall smaller and flatter group delay in the passband [19] and additionally allows the designer to independently control the filter selectivity or sharpness by accurately choosing the cut-off frequencies of the high-pass and low-pass filter sections.

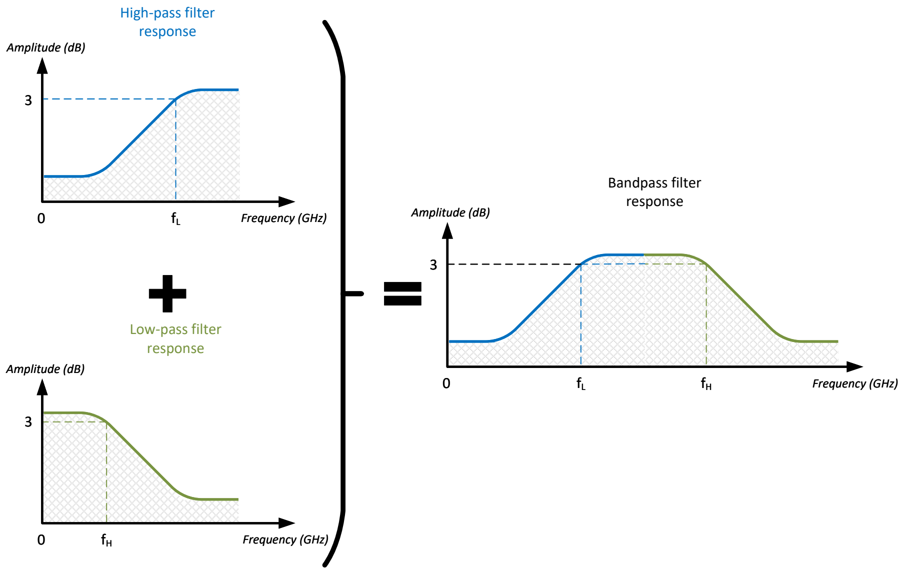

Figure 3.5: Conceptual view of cascaded low-pass high-pass filter response.

The basic single layer design utilises the synthesis equations presented in Chapter 2 to develop the equivalent circuits for the individual high-pass and low-pass sections. The integration of independently designed filters however has the risk of affecting the return loss of the resultant bandpass filter due to the interaction of phase at the joint, although this could be compensated for by adding a matched transmission line section to connect the high-pass and low-pass filter sections.

In [37] and [38] a novel microstrip UWB bandpass filter was successfully designed by cascading a high-pass and low-pass filter.

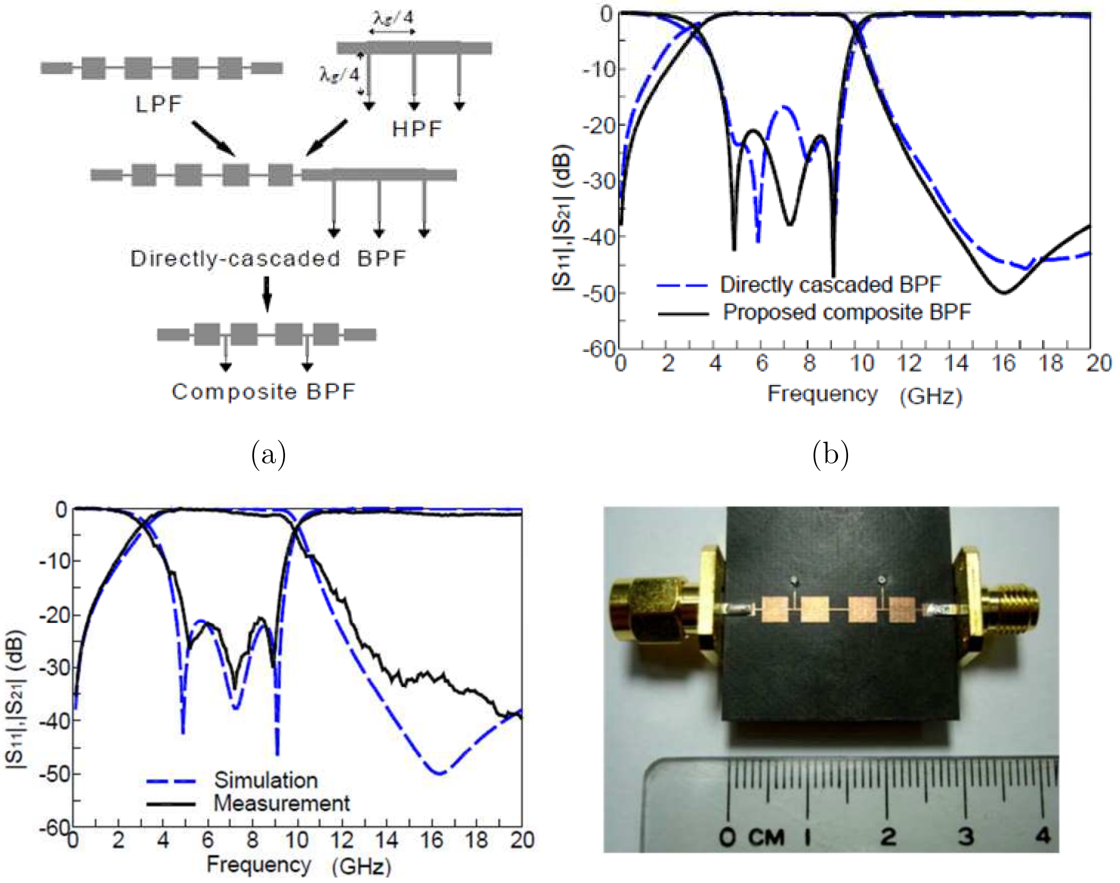

(a) (b)

(c) (d)

Figure 3.6: Cascaded High-pass-Low-pass Filter Topology: (a) Directly cascaded vs Embedded implementations (b) Simulated response of the directly-cascaded and embedded implementations (c) Simulated and measured response of the embedded implementation (d) Photograph of the manufactured embedded design [38].

Both designs utilises shunt quarter-wave short-circuited stubs to realise the high-pass filter section, but employs radial stubs and stepped impedance topologies respectively to realise the low-pass filter section. In [38], a correlation between having the individually designed sections directly cascaded and having them embedded into each other was presented as depicted in Figure 3.6(b). Both techniques achieve a 3 dB fractional bandwidth exceeding 100%, but the embedded technique has the advantage of occupying a much smaller overall circuit size as opposed to the directly cascaded technique. This type of design also has the benefit of easily being implemented on other planar structures such as stripline or suspended stripline as presented in [33].

This topology, albeit compact with good in- and out-of-band performance, would require a relatively high filter order to achieve the stringent selectivity specifications for the required anti-aliasing filter. This could as a consequence potentially lead to an increase in overall circuit size, despite having the option to embed the circuits as opposed to having them cascaded.

3.4 Multi-Mode Resonator (MMR) Filters

Single-mode resonator filters, such as those discussed in the previous sections, are designed such that the fundamental resonant frequency of the resonator(s) falls within the required passband, whilst widely spacing out the other resonant frequencies, and in so doing obtain a passband constituted only of one resonant frequency. Multi-mode resonator filters on the other hand, are designed by closely spacing the first few resonant modes into the wanted wide passband in order to achieve the desired response.

The concept of a multi-mode resonator filter with a stepped-impedance configuration was first reported by Zhu *et al.*in [39] where an aperture-backed single microstrip line resonator filter was used to develop an ultra-broadband bandpass filter. It achieved a fractional bandwidth of more than 70%, but the design concept was later adapted for UWB applications following the FCC's announcement in 2002 [40] where it then achieved a fractional bandwidth of about 109.5%.

The initial work presented in [39] used the first two resonant modes of the excited resonator to achieve the wide passband, whereas the later work needed to use the first three resonant modes to constitute the ultra-wideband passband response.

The basic resonator geometry is effectively a transmission-line resonator where both ends are open circuited. It consists of a low-impedance line section in the center and two identical high-impedance line sections on the two sides, as depicted in Figure 3.7. The physical implementation is the same as a conventional stepped-impedance resonator, but with one fundamental difference. For a MMR resonator configuration, the geometry is opposite to that of a conventional narrow-band stepped-impedance resonator (SIR) where it has a high-impedance line section in the middle and two low-impedance line sections on the two sides.

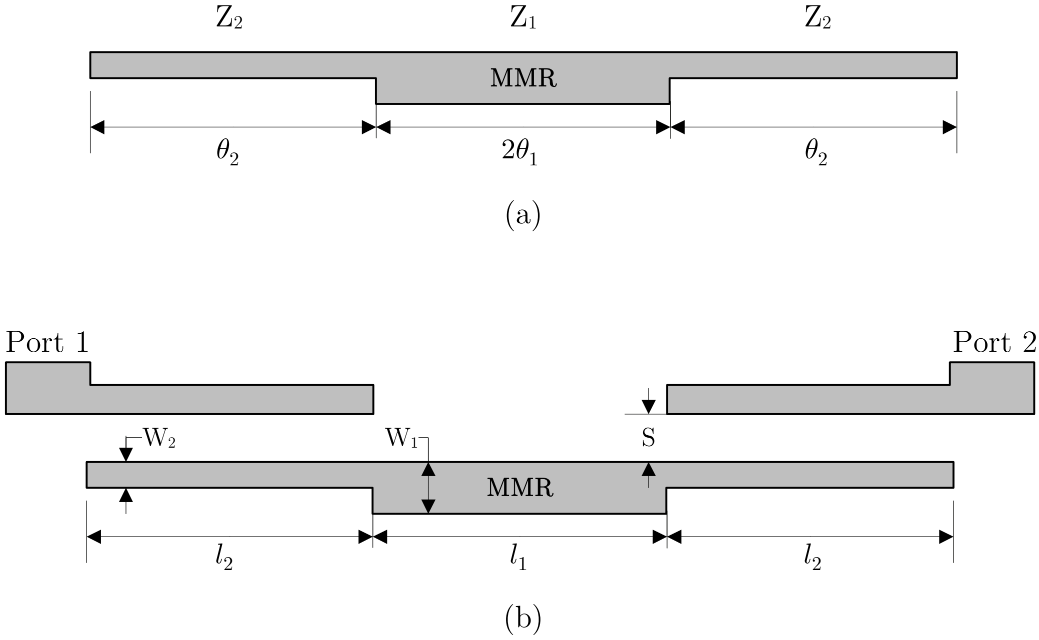

(a)

(b)

Figure 3.7: (a) Multimode stepped-impedance resonator filter (SIR), (b) Multimode SIR with I/O excitations [19].

Due to the particular geometry of the MMR, the first several resonant modes of the resonator can be exploited to design a UWB filter. The characteristic impedances of the high- and low-impedance line sections are denoted by Z_1 and Z_2, and the electrical lengths are denoted by θ_1 and θ_2 respectively. The impedance ratio of Z_2 to Z_1 is critical in the determining the position of the resonant frequencies, and is defined by $R = \frac{Z_2}{Z_1}$. The characteristic impedances Z_1 and Z_2 are chosen such that $R > 1$, where a smaller R tends towards the realization of a wider bandwidth of a multi-mode resonator filter. In the case where $\theta_2 = \theta_1 = \theta$, set of resonant frequencies can be obtained from [19]:

$$\begin{aligned} \theta\left(f_1\right) &= \tan^{-1}\sqrt{R} \\ \theta\left(f_2\right) &= \frac{\pi}{2} \\ \theta\left(f_3\right) &= \pi - \tan^{-1}\sqrt{R} \\ \theta\left(f_4\right) &= \pi \end{aligned} \tag{3.6}$$

Therefore, three normalised frequencies can be determined by

$$\begin{aligned}\frac{f_1}{f_2} &= \frac{2\tan^{-1}\sqrt{R}}{\pi} \\ \frac{f_3}{f_2} &= \frac{2}{\pi}\left(\pi - \tan^{-1}\sqrt{R}\right) \\ \frac{f_4}{f_2} &= 2\end{aligned} \tag{3.7}$$

And normalized resonant frequency separation between $\frac{f_1}{f_2}$ and $\frac{f_3}{f_2}$ can be determined as:

$$\Delta f_{13} = \frac{f_3 - f_1}{f_2} = \frac{2}{\pi}\left(\pi - 2\tan^{-1}\sqrt{R}\right) \tag{3.8}$$

The resultant Equation 3.7, is a set of normalised frequencies that has been normalized to f_2 due to it being selected as the center frequency for a multimode resonator filter making use of the first three resonant modes to constitute a wide passband. From Equation 3.7 it can also be seen that the fourth resonant frequency f_4, will always be twice the center frequency f_2, which could cause an unwanted spurious response close the desired passband when the bandwidth is wide.

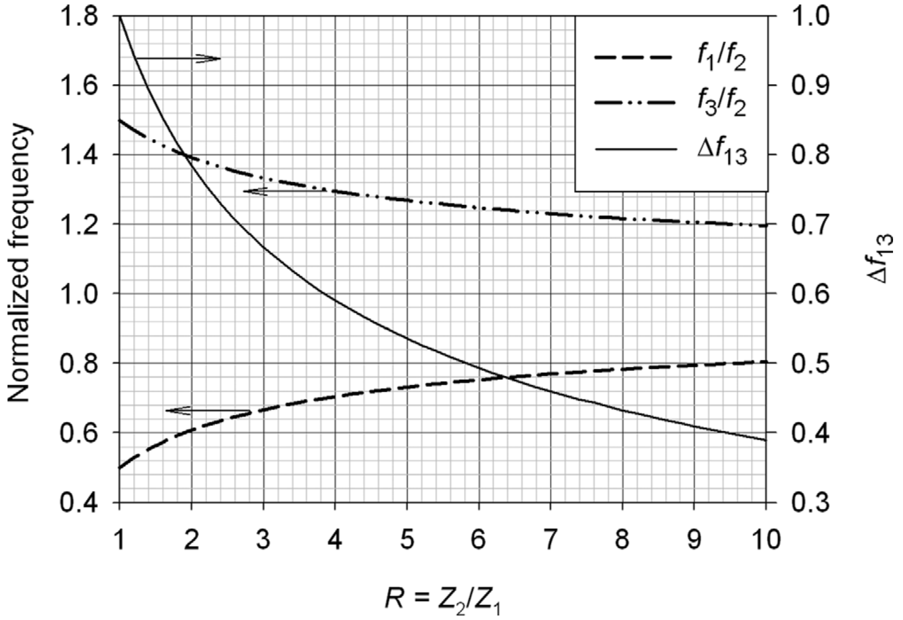

Figure 3.8: Normalised resonant frequencies versus impedance ratio R [19].

Equation 3.7 and 3.8 can also be plotted versus R to give a graphical representation of the resonant frequency separation for a given value of R. An example of such a plot is depicted in Figure 3.8. It is evident from the plot that for $R > 1$, the larger the impedance ratio R is between the high-impedance and low-impedance line sections, the narrower the filter bandwidth becomes. This highlights the importance of selecting the correct ratio of impedances for the respective line sections in order to achieve the desired bandwidth.

Further support to this rationale is presented in Figure 3.9 as an example. When the input and output ports of the MMR filter are weakly coupled, the first few resonant modes can be observed, where the coupling strength is determined by varying the coupling spacing s, as depicted in Figure 3.9 (a).

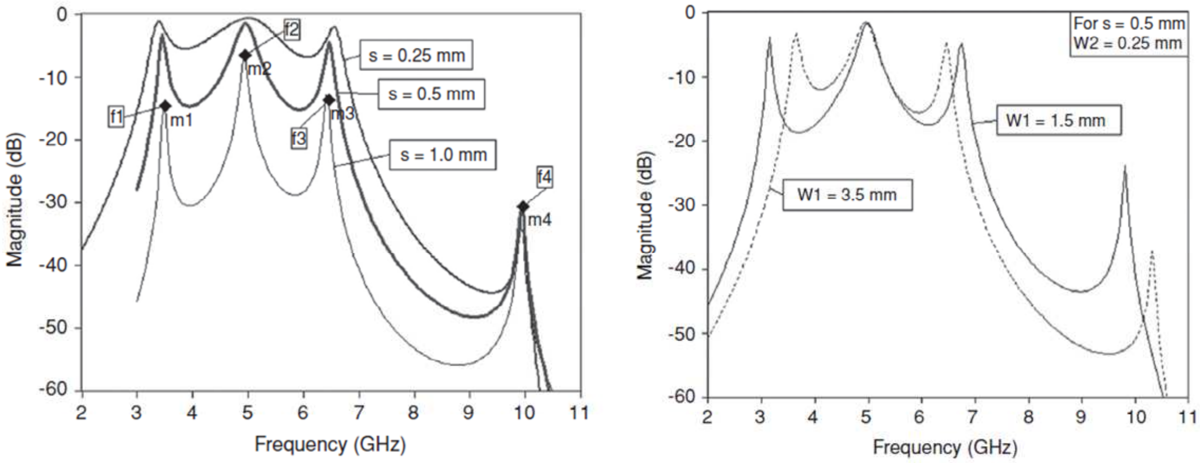

(a)

(b)

Figure 3.9: (a) Frequency response vs variation in coupling spacing, (b) Frequency response vs variation in width W_1 [19].

From Figure 3.9 (b) it can be seen that for a fixed high-impedance line section width of $W_2 = 0.25\ mm$ and a fixed coupling spacing of $s = 0.5\ mm$ for example, changing the low-impedance line section width W_1 varies the mode separation where an increase in W_1 tends to reduce the mode separation, and a decrease in W_1 increases the mode separation. This reaffirms that for $R > 1$, a larger R tends towards the realization of a narrower bandwidth multimode resonator filter [19].

Although the discussed SIR-based MMR bandpass filter exhibits a good ultra-wideband passband and compact circuit size, the physically realisable dimension of the coupling spacing could potentially be a challenge to achieve during manufacturing. This concern and potential problem is further compounded when incorporating parallel coupled microstrip lines with multiple MMR resonators which are capacitively coupled to achieve better selectivity. To circumvent this, the inclusion of an aperture formed in the ground plane is presented in [41]. In the next section a brief discussion on ground plane apertures and defected ground structures will be presented.

3.5 Performance Improvement Techniques

3.5.1 Filters using Ground Plane Aperture Techniques

The inclusion of a wide ground plane aperture (GPA) presented in [39] is a technique which uses a slot etched into the ground plane located directly underneath the coupled structure to achieve tighter coupling by effectively weakening the coupling between each conductor strip and the ground plane. In so doing, tighter coupling is achieved and allows for manufacturing tolerances to be eased. Further use of this technique is presented in [42] and [43] where tight coupling was required to achieve the required wide passband response, while additionally achieving an improved stopband response.

One of the drawbacks of using the GPA technique is that the width of the etched slot creates a significant effect on the characteristic impedance of the microstrip line, which in turn influences the return loss level [44].

In order to alleviate the problems associated with using ground plane apertures, a technique using a defected ground structure (DGS) was first reported by Park *et al.* [45]. The reported dumbbell shaped DGS design used two lattice shaped photonic band gap (PBG) cells etched into the microstrip ground plane, thereby creating a periodic defect. This defect changes the transmission line characteristics and causes a disturbance in the current distribution in the ground plane.

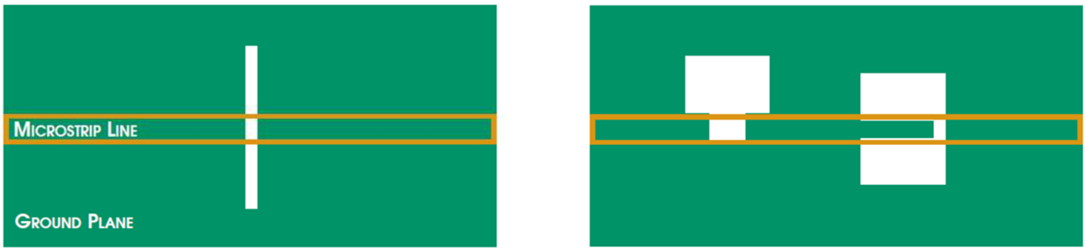

(a) Slot (c) Slot variations

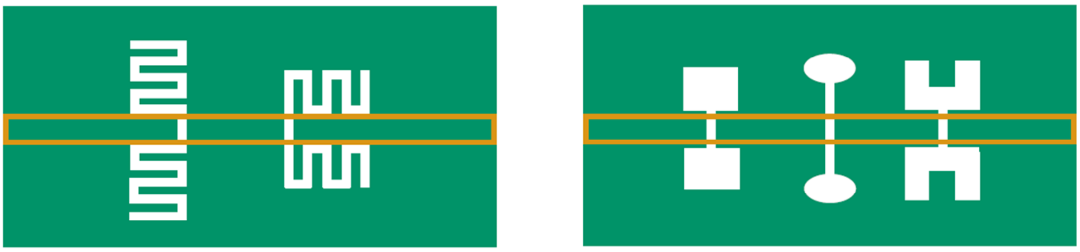

(c) Meandered lines (d) Various dumbbell shapes

Figure 3.10: Common configurations for DGS resonant structures [46].

The range of applicability to microwave filter designs has become apparent following the Park *et al.* report, and as a consequence many novel DGS designs have been proposed by researchers due to its attractive ability to suppress harmonics and also reduce the overall circuit size [47]. Examples of various implementations are depicted in Figure 3.10.

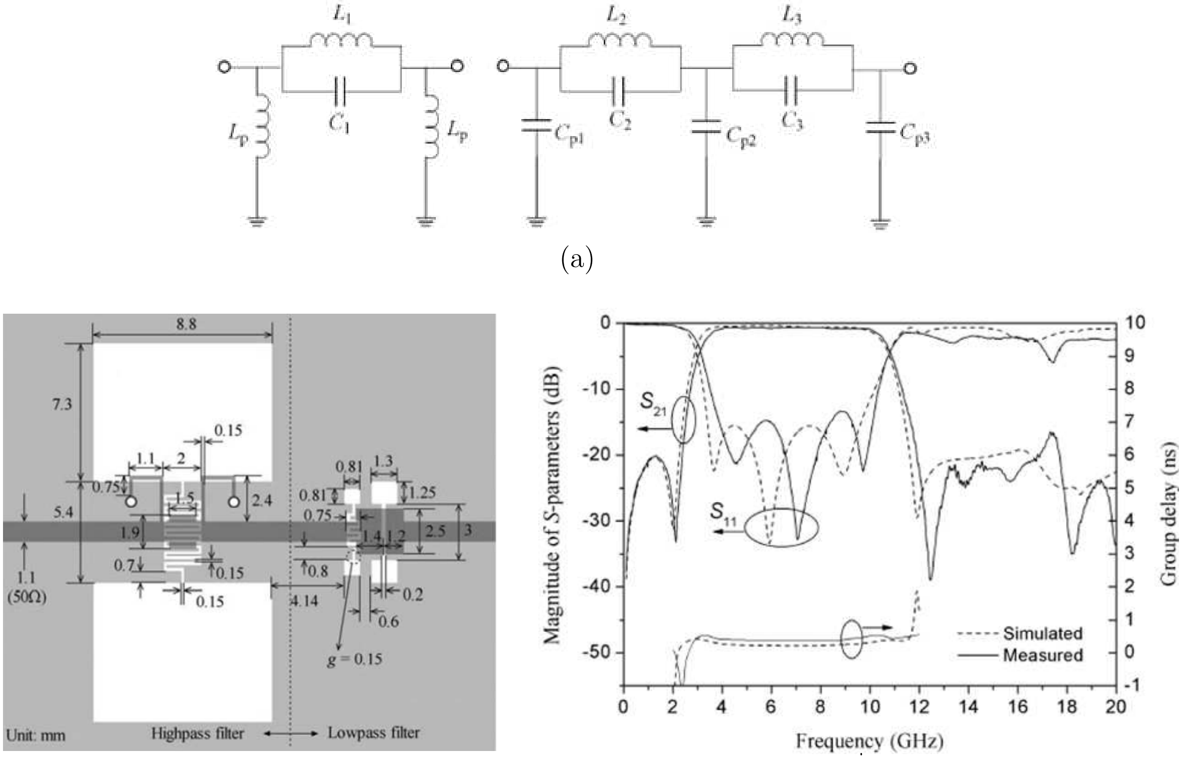

(a)

(b)

(c)

Figure 3.11: Cascaded High-pass Low-pass Topology using a DGS (a) High-pass Low-pass prototype (b) Configuration of designed filter (c) Measured results of the fabricated filter [48].

The design in [48] utilises this technique to improve the stopband rejection. A dumbbell shaped defected ground structure (DGS) was used to physically implement the parallel LC resonators. Furthermore, the design incorporated a meandered transmission line to connect the band gap cells, therein allowing a reduction in the overall occupied circuit size. Apart from achieving a 3 dB fractional bandwidth of 108% and an insertion loss of 0.9 dB over the passband, the design also exhibits good selectivity, especially at the upper transition. The design furthermore achieved a upper stopband rejection of more than 20 dB from 10.65 GHz to 16.8 GHz.

The periodic slots which forms the defected ground structure significantly aids in enhancing the coupling strength and providing an increase in harmonic suppression, but as a consequence, the technique has the disadvantage of radiation emanating through those slots, resulting in an increase in radiation losses. Even though most of the incident energy at resonance is reflected back down the transmission line, there is still significant radiation [46]. Radiation within enclosed microwave circuits can be difficult to include in simulation, and in some case the size of the enclosure makes the problem too large for EM solvers to achieve a solution within a reasonable time.

3.5.2 Filters using Suspended Stripline

Suspended stripline (SSL), which is a modified version of stripline, is planar type of transmission line which was first described by Rooney and Underkoefler in 1978 [49] and has since proven to be essential to the design of reasonably low-loss very broad-band filters.

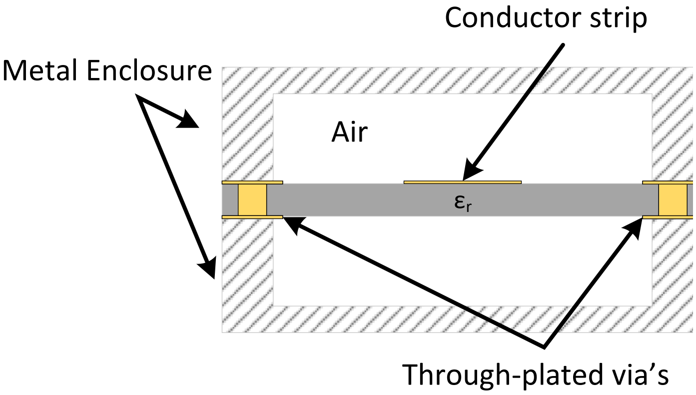

Figure 3.12: Cross-sectional view of a suspended stripline structure.

Figure 3.12 depicts the cross-sectional view of a basic suspended stripline structure. The conducting strip is placed on the surface of a thin dielectric substrate, where the substrate is suspended in air which is supported and enclosed in a metallic enclosure. Due to the confinement of the structure, a uniform dielectric (air) is formed, allowing the EM wave propagation to be purely TEM. As such, the electric and magnetic components of the EM wave is traversal to the direction of propagation. The plated through-holes (vias) in the area of the metallic enclosure walls provides a grounding connection between to upper and lower halves of the enclosure in order to maintain a conductive connection, thereby fully eliminating radiation losses [50].

Suspended stripline has proven to be an excellent transmission-line system to physically realize different types of filter implementations. When compared to filters using microstrip, it offers reduced losses and a higher Q-factor. It however does have the disadvantage of being larger in size and requires and increased fabrication effort due to the criticality of the metallized enclosure.

Different types of filter implementations using suspended stripline can be found in literature

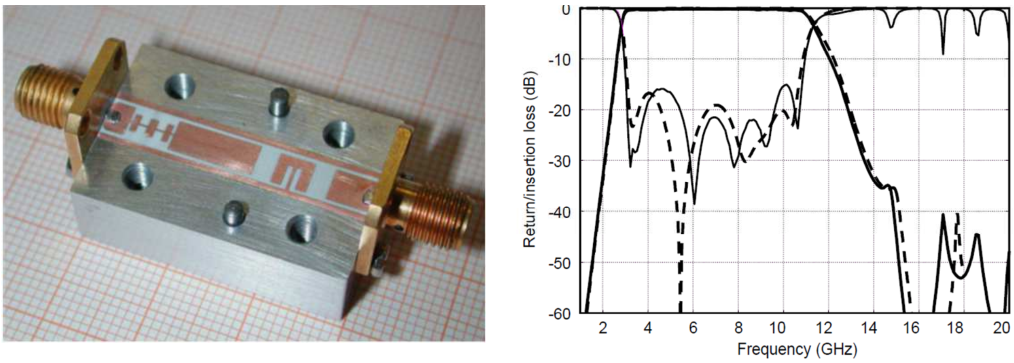

(a) (b)

Figure 3.13: (a) Photograph of fabricated SSL bandpass filter, (b) Measured performance response of the SSL filter [33].

[51][33]. In [33] a low-loss ultra-wideband filter is presented using suspended stripline. The filter uses a cascaded low-pass high-pass configuration based on conventional filter theory. The low-pass and high-pass sections of the filter is implemented on the suspended stripline structure, where the broadside coupled patches are used to implement capacitances and the short circuited stubs are adopted to implement inductances [29]. To improve the resultant return loss when combining the two filter sections, a transmission line section was incorporated between the two filter sections to improve of the overall return loss. The realized filter, depicted in Figure 3.13(a), The filter performance shows good correlation between the simulated and measured results as depicted in the Figure 3.13(b) where it achieved a low insertion loss of 0.4 dB over the passband from 4 GHz to 10.6 GHz.

3.5.3 Multilayer Structured Filters

The development of advanced packaging materials such as liquid crystal polymer technology (LCP) and low-temperature co-fired ceramic technology (LTCC) has allowed for the exploitation of multilayered circuit technologies to design and implement ultra-wideband filters with compact sizes. These packaging materials also allows multi-layered broadside coupled techniques to be easily implemented, since very strong coupling between the input/output ports as well as the inner sections are required when designing ultra-wide bandpass filters [19]. A brief discussion about these materials are discussed in the next sections.

3.5.3.1 Liquid Crystal Polymer Technology (LCP)

Liquid crystal polymer technology (LCP) is an organic thermoplastic polymers which can be used as a substrate, a superstrate as well as a packaging material. It has an extremely low moisture-absorption characteristic which allows it to maintain stable electrical and mechanical properties in a fairly humid environment [19]. Its excellent electrical properties, such as being stable and having a low dielectric constant and dissipation factor makes it well suited for use as a substrate material for microwave applications. Other benefits of using LCP technology includes a compact integration, flexibility and a relatively low manufacturing cost which is similar to that of conventional printed circuit boards such as FR4 [52]. Liquid crystal polymer technology can be used in a multi-layered structure (MLCP) in order to achieve a compact multilayer laminate circuit. An example of a typical multilayer stack-up is shown in Figure 3.14, where two types of LCP films, namely the bonding film and the core film, are used in the manufacturing process. During manufacturing the entire stack is compressed and heated where the bonding film is melted causing it to chemically bond to the core film.

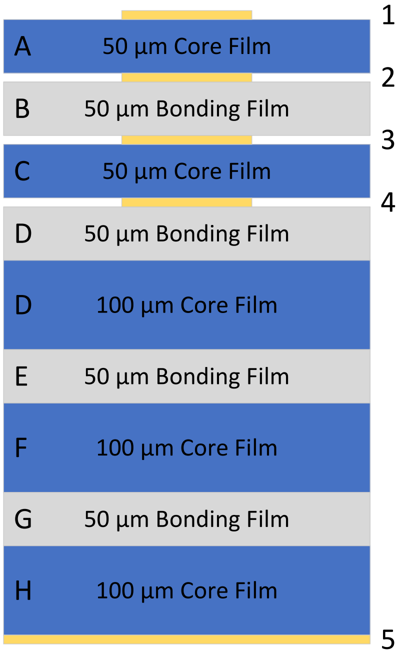

Figure 3.14: Typical stack-up of a multi-layer LCP structure [53].

An example of a ultra-wideband filter using multilayer LCP technology is presented in [54] where a miniaturised cascaded low-pass high-pass filter configuration was constructed using LCP technology. It achieved a very densely packaged circuit size of 5.1 mm x 8.86 mm and obtained an insertion loss 0.35 dB ± 0.15 dB from 3.9 to 9.3 GHz.

Another example is presented in [32], where a quasi-lumped element bandpass filter was designed and built using multilayer LCP technology. The 3-D structure of the designed filter is depicted in Figure 3.15. The geometry of the implemented filter uses broadside-coupled radial patches to represent series capacitance which is realised on two different metal layers, namely the top and middle layers. The series inductors are implemented by high impedance microstrip line sections and the shunt inductor is implemented by using a short-circuited microstrip which has been realised as a large pad. The designed filter exploits the benefit using LCP technology where thin dielectric LCP substrates with thicknesses of 0.1 mm (h1) and 0.7 mm (h2) were used, which facilitated the implementation of the larger series capacitances. This filter achieved a minimum insertion loss of 0.35 dB over the passband from 3.6 to 10.2 GHz.

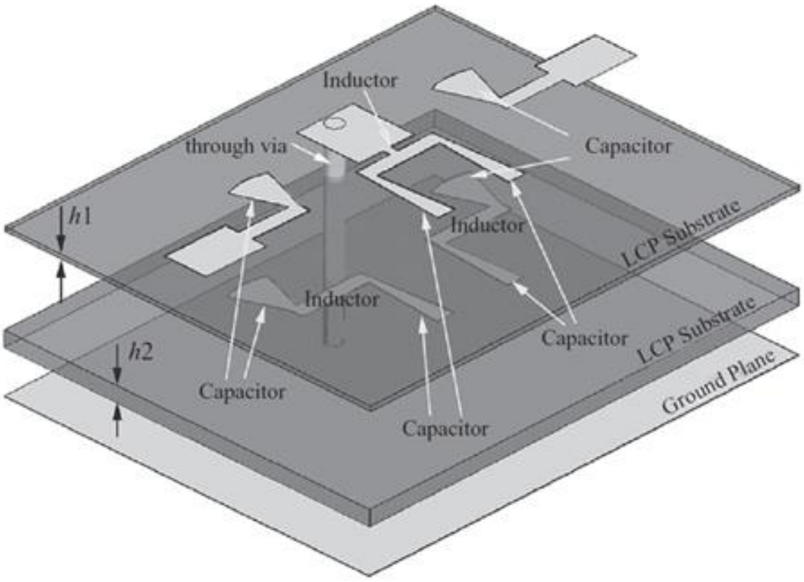

Figure 3.15: 3D structure of designed UWB bandpass filter [32].

It is important to note that LCP is a polymer and is not intended to completely replace any conventional materials such as FR4, Duroid, LTCC or alumina, but for many applications it offers a distinct advantage, such as [55]:

- Having low-loss at operating frequencies exceeding X-Band,
- Being as flexible as paper, making it ideal for use in conformal electronics applications, and
- Being able to achieve very compact overall circuit sizes when using a multi-layered approach where it can be used as a substrate and packaging material.

3.5.3.2 Low-temperature co-fired ceramic (LTCC) Technology

Low-temperature co-fired ceramic (LTCC) is a glass-ceramics composite which offers many benefits to designs which require flexibility, compactness and reliability. It can be used in a multi-layered implementation which allows multiple circuitry to be handled in a self-contained, hermetic package [19]. The versatility of a LTCC structure can be illustrated by it's ability to incorporate buried components. As an example, LTCC provides a mechanism for microstrip, stripline, coplanar waveguide and DC lines, to be all integrated within the same medium. This largely reduces the assembly complexity and increases system reliability due to the reduced number of solder joint interconnections.

Other benefits of LTCC technology include the low loss characteristic of the dielectric and the hermetic ceramic structure which eliminates any concerns relating to moisture ingress to moisture related failures [56]. Looking past the attractive features, the main drawback of LTCC technology is its fabrication cost when compared to LCP technology and conventional printed circuit boards.

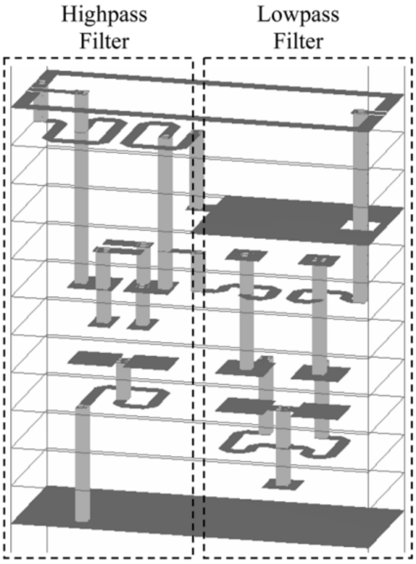

Figure 3.16: 3D structure of designed multilayer LTCC wideband filter [57].

The design and fabrication of a LTCC wideband bandpass filter is presented in [57]. The design is realised by cascading low-pass and high-pass filter sections on a multilayer LTCC structure. The low-pass filter section was fabricated on eight layers and the high-pass filter section was fabricated on 11 layers, and achieved a compact overall circuit size of 6.5 x 2.5 x 1 mm operating at 3.1–4.9 GHz. The 3-D structure of the designed filter is depicted in Figure 3.16.

3.6 Filter Technology Summary

A brief overview of various applicable microwave filter technologies and topologies capable of meeting the required specifications has been presented in this chapter. Many of the reported techniques uses single-layered microstrip technology, such as the quarter wave length shunt short-circuited stub technique, the cascaded high-pass/low-pass technique, as well as the multi-mode resonator (MMR) technique.

Furthermore, it was reported that certain performance parameters of the aforementioned techniques could be improved on when employed in conjunction with certain enhancement techniques, such as, incorporating a ground plane aperture or variants thereof.

The option of suspended stripline transmission line was also presented, as well as multi-layered structures such as those using liquid crystal polymer (LCP) and low-temperature co-fired ceramic (LTCC) technology substrates. It was found that the single-layered microstrip technology has merits of relatively low cost and ease of fabrication, whereas the multi-layered technology has the advantage of small circuit size with more functionality [29].

Table 3.2: Presented filter technologies comparison

Technology/Technique		**Advantages**	**Disadvantages**
Single-layered	Quarter-wave shunt short-circuited stubs [3]	- Easy to fabricate - Good selectivity	- Spurious harmonic at $2f_0$
	Cascaded LP/HP [37] [38]	- Wide upper stopband rejection	- Larger circuit size - Degraded insertion loss
	MMR [40]	- Compact size	- Requires tight coupling which may be hard to physically realise
	SSL [33]	- Low loss - Wide upper stopband rejection	- More expensive to manufacture - Larger in size
	DGS [48]	- Reduced circuit size	- Higher radiation losses - May require longer simulation time
Multi-layered	Filters using LCP technology [54] [32]	- Compact size - Low loss	- More complex design - Increased manufacturing complexity
	Filters using LTCC technology [57]	- Compact size - Low loss	- Expensive to manufacture

A brief description of the advantages and disadvantages for each of the presented filter technologies is tabulated in Table 3.2. Although each technology and/or technique has merits worth noting, after careful consideration between a wide variety of factors including those presented in this chapter, the technology opted for to design the required anti-aliasing filter was the quarter-wave shunt short-circuited stub implemented on microstrip due to the ease in fabrication and circuit integration.

Chapter 4

Design of Anti-aliasing Filter

4.1 Filter Response and Order

One of the design decisions that is required to be made early on in the filter realisation process is the selection of the filter's transfer function. The typically-used transfer functions which are considered for this design, namely Butterworth and Chebyshev, have been already briefly addressed in Chapter 2. If the desired filter response is not specified, which is the case in this instance, the decision usually involves a design trade-off.

For consideration: filters with a Butterworth response have no passband ripple. Additionally the insertion loss is flat in the passband and increases monotonically with frequency. On the other hand, filters with a Chebyshev response provide better selectivity and out-of-band rejection depending on the permissible passband ripple [58]. In this decision lies yet another, since an increase in passband ripple results in better selectivity, but at the cost of an increase in insertion loss.

For ease of reference, the design specifications in Table 1.1 is repeated here:

Table 4.1: Anti-aliasing Filter Specifications

Parameter	**Specification**
Passband	3.25 GHz - 5.75 GHz
Bandwidth	2.5 GHz
Insertion Loss	$\leq$ 2 dB
Return Loss	$\geq$ 10 dB
Fractional Bandwidth	55.6 %
Stopband attenuation	$\geq$ 23 dB
Lower stopband frequency	2.75 GHz
Upper stopband frequency	6.25 GHz

For a Butterworth response; the filter order can be determined from Figure 2.1, or it can be determined analytically from Equation 2.13 as

$$n \geq \frac{\log\left(10^{0.1L_{As}} - 1\right)}{2\log\Omega_s}$$

$$n \geq \frac{\log\left(10^{0.1\times 30} - 1\right)}{2 \times \log\left(\frac{6.25}{4.5}\right)}$$

$$n \geq 10.512$$

where:

n is the required filter order, rounded upwards to the next integer value if not an integer,
L_{As} is the stopband attenuation, and
Ω_s is the stopband frequency.

For a Chebyshev filter response, the passband ripple would have to be known before the filter order can be determined. As is the case in this design, there are instances where the minimum passband return loss L_R is specified instead of the minimum passband ripple [19]. As such, the corresponding passband ripple L_{Ar} can be determined from Equation 4.1.

$$L_{Ar} = -10\log\left(1 - 10^{0.1L_R}\right)\ dB \qquad (4.1)$$

The above calculation yields a passband ripple result of 0.458 dB for the specified minimum passband return loss of 10 dB. Since the filter PCB is to be connectorised, it is expected that the return loss may be degraded as a consequence, hence a Chebyshev filter response having a more stringent passband ripple of 0.01 dB is considered.

Similarly then, for a Chebyshev response; the filter order n can be approximated from the attenuation curves for a passband ripple of 0.01 dB such as those in Figures 2.2 and 2.3, from [21], or analytically by using Equation 2.14.

$$n \geq \frac{\cosh^{-1}\sqrt{\frac{10^{0.1L_{As}}-1}{10^{0.1L_{Ar}}-1}}}{\cosh^{-1}\Omega_s}$$

$$n \geq \frac{\cosh^{-1}\sqrt{\frac{10^{0.1\times 30}-1}{10^{0.1\times 0.01}-1}}}{\cosh^{-1}\times(\frac{6.25}{4.5})}$$

$$n \geq 8.395$$

where the stopband attenuation L_{As} was chosen to be 30 dB in either filter response case. From this comparison, it can be seen that for a Butterworth response, a 11^{th} order filter would be required as a minimum to achieve the required selectivity, whereas for a Chebyshev response having a 0.01 dB passband ripple, a 9^{th} order filter would be required.

In order to achieve a compact design, the Chebyshev response was opted for in the filter design.

4.2 Bandpass Filter Design

The approach to designing a quarter wave shunt short circuited stub bandpass filter in [21] is somewhat different to the conventional design methods and those presented in Chapter 2. The design procedure makes use of the closed-form Equations 3.3 to determine the required characteristic admittances of the transformed and converted quarter wave shunt short circuited stub bandpass filter depicted in Figure 3.2. The rationale behind the difference in design approach is so that a practical stub filter with realisable characteristic admittances can be designed and built.

The design starts with a low-pass prototype filter, where the element values (g values) were obtained for a 9^{th} order Chebyshev filter response having a passband ripple of 0.01 dB from tables in [21] as:

$$
\begin{aligned}
g_0 = g_{10} &= 1 \\
g_1 = g_9 &= 0.8144 \\
g_2 = g_8 &= 1.4270 \\
g_3 = g_7 &= 1.8043 \\
g_4 = g_6 &= 1.7125 \\
g_5 &= 1.9057
\end{aligned}
$$

Once the element values and fractional bandwidth (FBW) are known, the normalised low-pass filter prototype filter can be transformed to have the form depicted in Figure 4.1, where the characteristic admittances can be calculated in a straight forward manner using Equations 3.3. All the stubs and transmission line sections are $\lambda_g/4$ long at 4.5 GHz, where the $\lambda_g/4$ transmission line sections between the stubs act as admittance inverters [18].

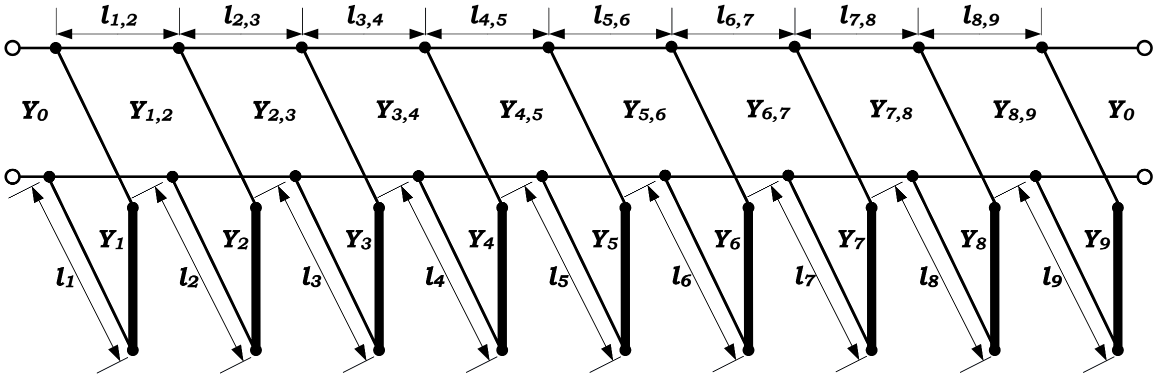

Figure 4.1: Transmission line model for a 9^{th} Order Chebyshev bandpass filter with shunt short-circuited stubs.

In the equations, there is a dimensionless constant h, which was chosen as $h = 2$ in order to achieve acceptable admittance levels in the interior of the filter. Table 4.2 summarises the calculated transmission line admittances for the design using an $n = 9$ reactive element Chebyshev prototype with a 0.01 dB passband ripple.

The circuit simulations for this design were done using the commercial CAD package, AWR [59]. Figure 4.2 shows the circuit model layout of the designed 9^{th} order Chebyshev bandpass filter with shunt short-circuited stubs using ideal transmission line models, whilst Figure 4.3 plots the filter's insertion (S_{21}) and return loss (S_{11}) which were obtained by simulation.

Note in Table 4.2 that the characteristic admittances of the end stubs, namely Y_1 and Y_9, are approximately half that of the stubs in the interior of the filter. For this reason the design

Table 4.2: Calculated parameters for the $\lambda_g/4$ shunt short-circuited stub filter transmission line model

$\boldsymbol{i}$	$\boldsymbol{\frac{J_{i,i+1}}{Y_0}}$	$\boldsymbol{Y_i}$ (℧)	$\boldsymbol{Z_i}$ ($\boldsymbol{\Omega}$)	$\boldsymbol{Y_{i,i+1}}$ (℧)	$\boldsymbol{Z_{i,i+1}}$ ($\boldsymbol{\Omega}$)
1	1.068	0.020	51.074	0.021	46.800
2	1.015	0.040	25.202	0.020	49.257
3	0.927	0.041	24.326	0.019	53.960
4	0.902	0.042	23.648	0.018	55.456
5	0.902	0.043	23.499	0.018	55.456
6	0.927	0.042	23.648	0.019	53.960
7	1.015	0.041	24.326	0.020	49.257
8	1.068	0.040	25.202	0.021	46.800
9	-	0.020	51.074	-	-

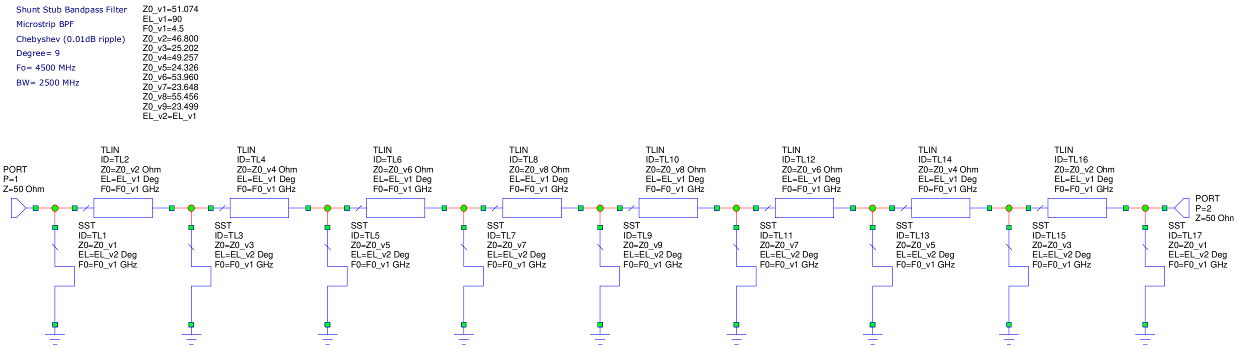

Figure 4.2: Circuit Model using ideal transmission line components for the 9^{th} Order Chebyshev bandpass filter.

was modified to adopt double parallel stubs in the interior of the filter which have double the impedance of the calculated impedance whilst maintaining the single stubs at the end. Table 4.3 summarises the transmission line admittances and impedances having the form depicted in Figure 4.4, and Figure 4.5 plots the filter's frequency response obtained by simulation.

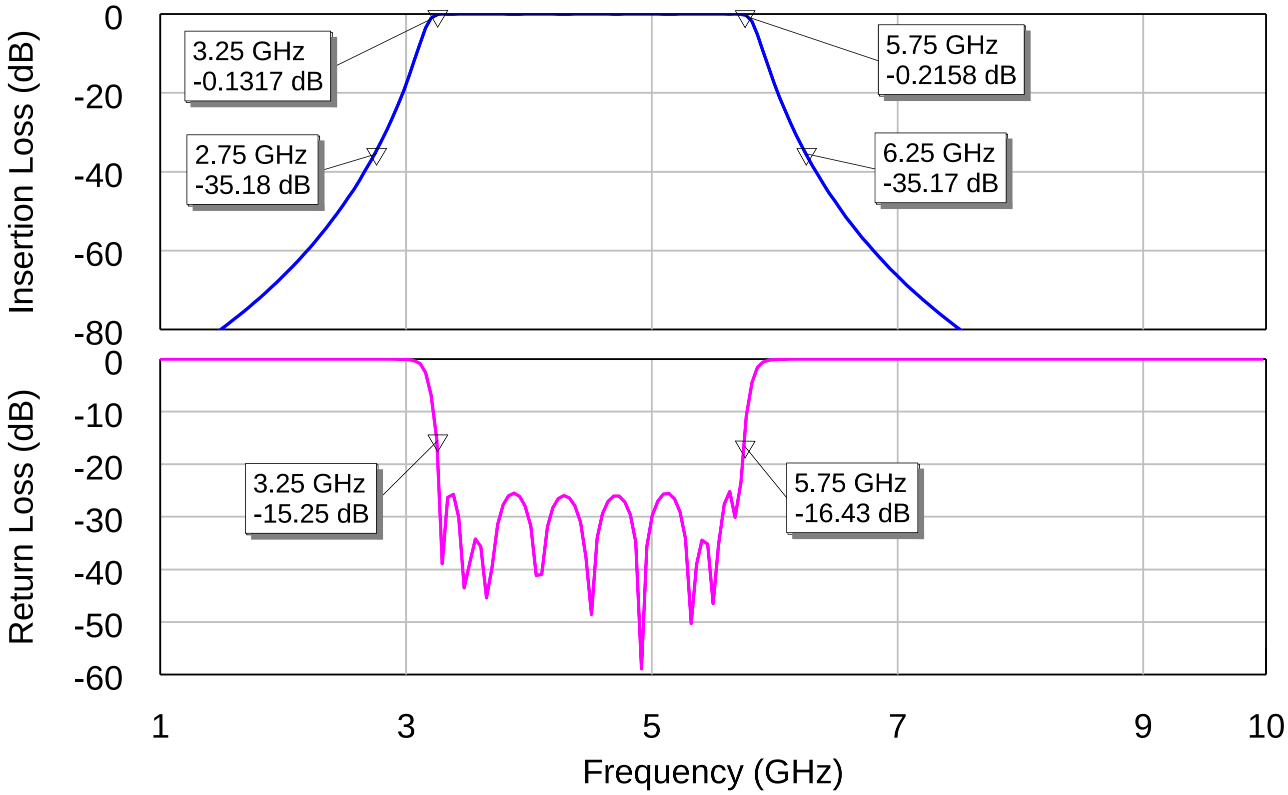

Figure 4.3: Circuit Model Plot using ideal transmission line components for the 9^{th} Order Chebyshev bandpass filter.

Table 4.3: Calculated parameters for double stub filter

$\boldsymbol{i}$	$\boldsymbol{Y_i}$ ($\mho$)	$\boldsymbol{Z_i}$ ($\boldsymbol{\Omega}$)
1	0.020	51.074
2	0.020	50.404
3	0.021	48.652
4	0.021	47.296
5	0.022	46.998
6	0.021	47.296
7	0.021	48.652
8	0.020	50.404
9	0.020	51.074

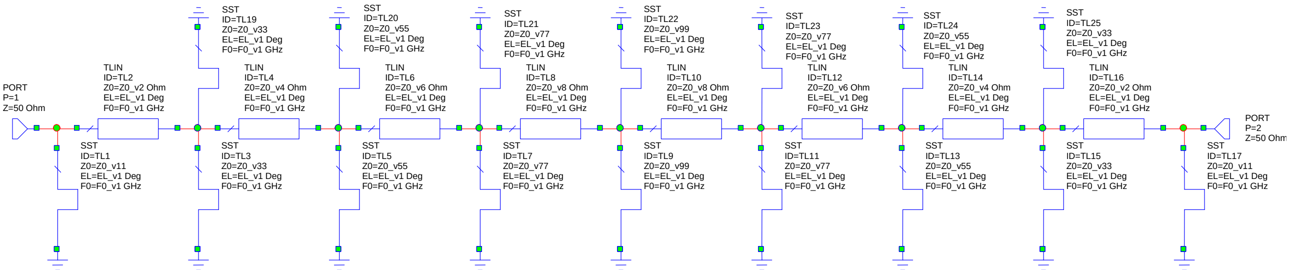

Figure 4.4: Circuit Model using ideal transmission line components and double stubs.

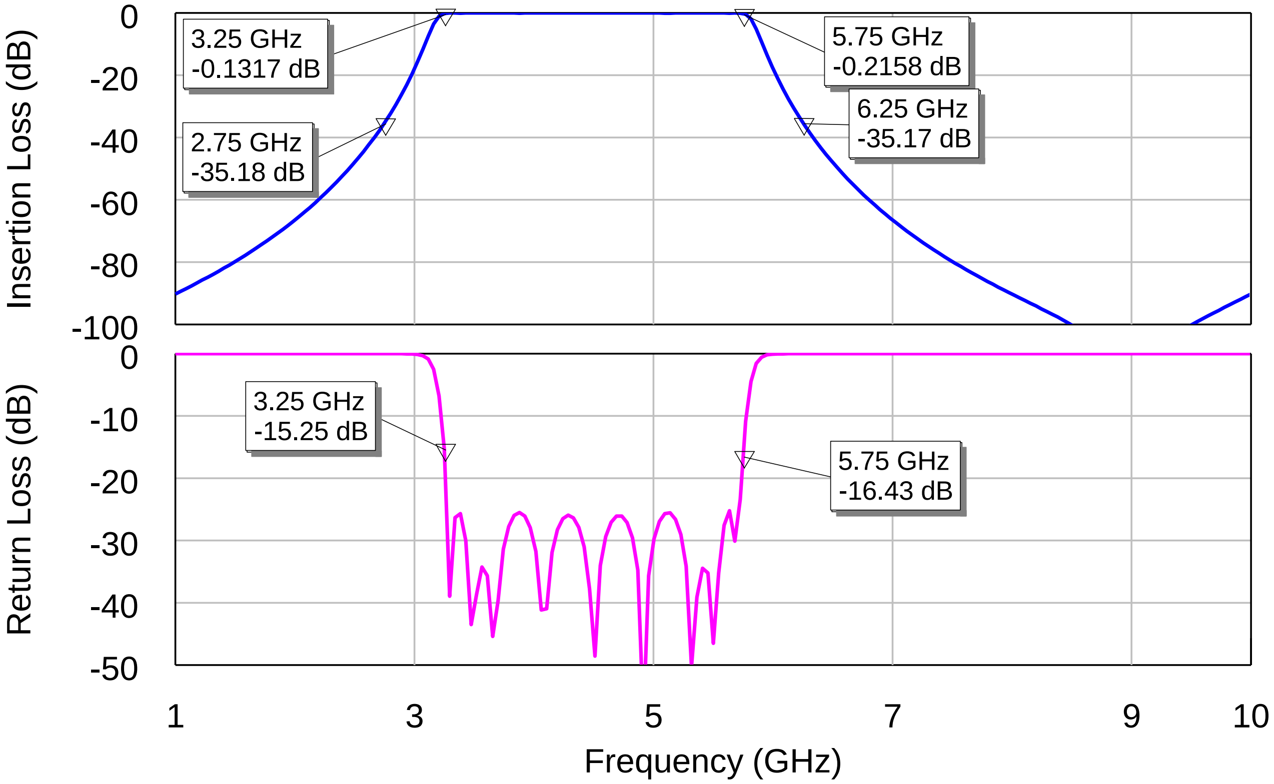

Figure 4.5: Circuit Model Plot using ideal transmission line components and double stubs.

4.3 Bandpass Filter Realisation

For the realisation of the microstrip filter design, Rogers RT6010LM [60] was used as the dielectric substrate. It has a relative dielectric constant of $\varepsilon_r = 10.7$, a dielectric loss tangent of $\tan\ \delta = 0.0023$ where the substrate thickness of $h = 1.27\ mm$ was chosen with copper thickness of 18 μm. The transmission line widths can be calculated using the microstrip design equations presented in Chapter 2, with the guided quarter-wavelengths associated with the characteristic impedances in Table 4.2 being calculated using Equation 4.2. The calculated transmission line widths and lengths are summarised in Table 4.4.

$$\lambda_g = \frac{c}{f_0\sqrt{\varepsilon_e}} \tag{4.2}$$

Table 4.4: Calculated transmission line lengths and widths for the designed bandpass filter

Transmission Line	**Width (mm)**	**Length (mm)**
TL1, TL17	1.077	6.156
TL3, TL15, TL19, TL25	1.109	6.147
TL5, TL13, TL20, TL24	1.196	6.123
TL7, TL11, TL21, TL23	1.269	6.103
TL9, TL22	1.286	6.099
TL2, TL16	1.297	6.096
TL4, TL14	1.165	6.131
TL6, TL12	0.952	6.194
TL8, TL10	0.893	6.213

Figure 4.7 shows the layout of the designed microstrip bandpass filter using AWR, where the transmission line lengths and widths were required to be optimised in order to incorporate the junction effects of where the stubs and mainline transmission lines meet. Additionally, the connection between the shunt stubs to the ground plane using vias adds inductance which changes with frequency [61], which also required optimisation. The passband, return loss and out-of-band rejection optimisation goals which were used in the simulation was selected to be in-line with the specifications presented in Table 4.1. Table 4.5 summarises the optimised transmission line lengths and widths where each shunt stub was short-circuited using a 0.3 mm diameter via hole. The diameter of the via hole was chosen as a consequence of the narrowest transmission line trace, namely 0.578 mm. Figure 4.6 plots the filter's frequency response where it can be seen that the performance is in good correlation with the design objective so far, despite the spurious harmonic around $2\omega_0$. It can also be seen that the return loss is

degraded when compared to the circuit model plot in Figure 4.5, which is likely due to effects caused by the addition of the vias.

Table 4.5: Optimised transmission line lengths and widths for the designed bandpass filter

Transmission Line	Width (mm)	Length (mm)
TL1, TL17	1.179	5.768
TL3, TL15, TL19, TL25	0.578	5.431
TL5, TL13, TL20, TL24	1.460	4.329
TL7, TL11, TL21, TL23	1.295	5.126
TL9, TL22	1.132	5.758
TL2, TL16	1.344	5.505
TL4, TL14	1.378	5.933
TL6, TL12	1.458	5.710
TL8, TL10	1.037	4.231

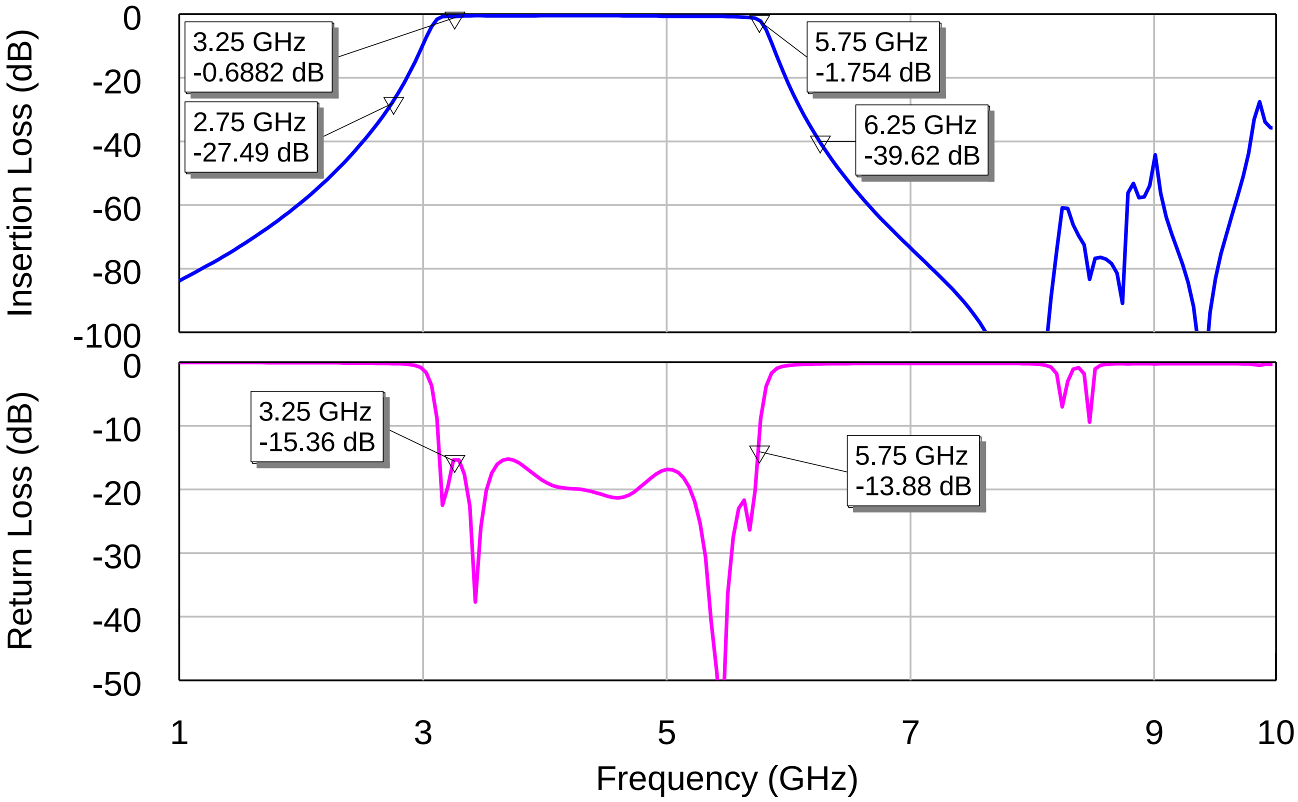

Figure 4.6: Circuit Model Plot using realistic transmission line components for the 9^{th} Order Chebyshev bandpass filter.

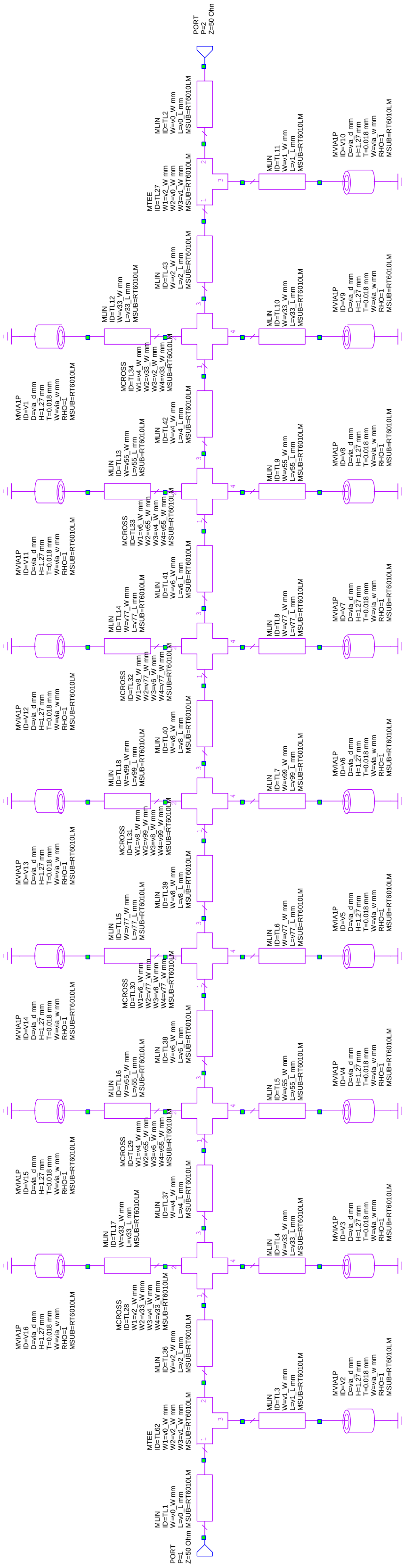

Figure 4.7: Circuit Model using realistic transmission line components for the 9^{th} Order Chebyshev bandpass filter.

4.4 Electromagnetic (EM) Simulations

The full-wave electromagnetic (EM) simulation of the circuit design was done using CST Studio Suite [62], which is a 3D modelling and EM analysis software package used to analyse and optimise the EM microstrip structure. For the analysis, CST's Frequency Domain Solver was used as recommended by CST when simulating highly resonant structures such as Bandpass Filters and Diplexers [63], which is based on the finite element method (FEM).

The constructed 3D model of the designed bandpass filter is depicted in Figure 4.8. In the 3D model, the short circuiting of the shunt stubs are represented by cylindrical vias which are connected from the top transmission lines down to the ground plane. The transmission line lengths and widths were optimised in order to achieve the required passband from 3.25 - 6.25 GHz with a return loss of $\geq$ 10 dB. The optimised transmission line lengths and widths are summarised in Table 4.6.

The simulated result is depicted in Figure 4.9 where it can be seen that the passband and return loss specifications are achieved. The simulated results also shows that the filter achieves an out-of-band rejection better than 30 dB up to 10 GHz. It should however be noted that although the simulated return loss of 10.12 dB meets the specifications, it is not ideal as the tolerances involved in the manufacturing of the filter could lead to a degraded measurement result.

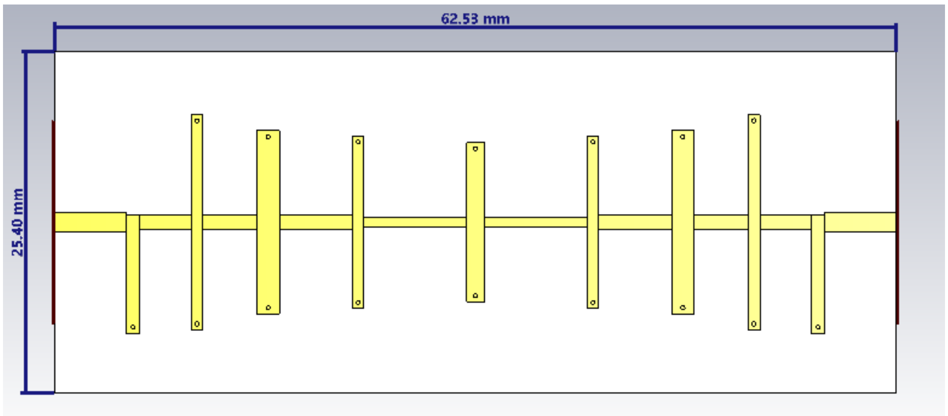

Figure 4.8: 3D model of the designed bandpass filter with no enclosure.

It was required that the final filter structure be housed in a metallic enclosure in order to provide shielding. The shielding provided by the enclosure is intended to contain the radiation emanating from the circuit and also prevent external interfering signals from coupling into the circuit. The inclusion of the metallic enclosure provides an additional benefit of providing mechanical rigidity to the overall microstrip structure. Although the

Table 4.6: Optimised EM microstrip structure line lengths and widths with no enclosure

Transmission Line	Width (mm)	Length (mm)
TL1, TL17	1.02	8.78
TL3, TL15, TL19, TL25	0.88	8.00
TL5, TL13, TL20, TL24	1.68	6.80
TL7, TL11, TL21, TL23	0.87	6.395
TL9, TL22	1.29	5.92
TL2, TL16	1.07	3.82
TL4, TL14	1.09	4.00
TL6, TL12	1.05	5.42
TL8, TL10	0.79	7.64

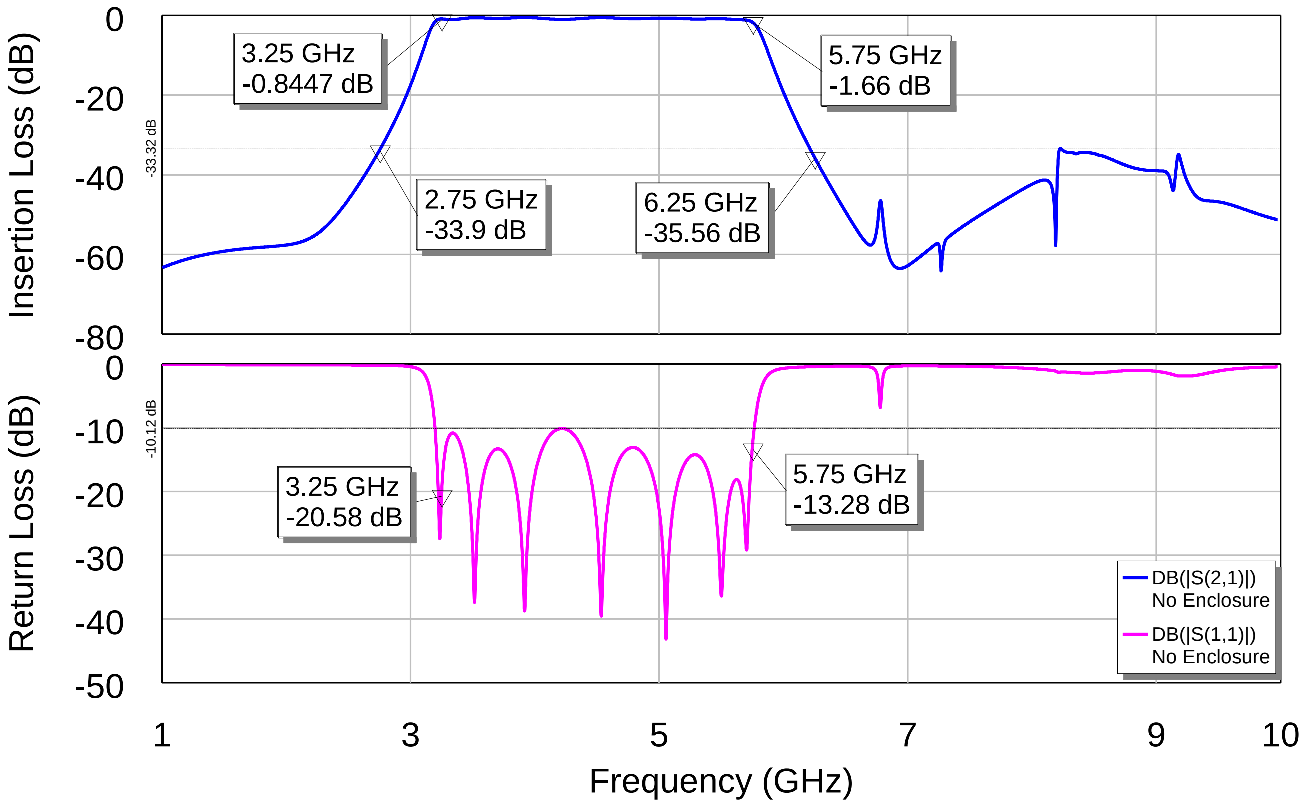

Figure 4.9: Optimised EM simulation plot of the designed bandpass filter with no enclosure.

provided enclosure was previously manufactured and used for a different filter design, the dimensions are adequately suited to house this specific filter design. Further optimisation was done with the provided metallic enclosure due to the effect it has on both the characteristic impedance and effective dielectric constant caused by the conducting side walls of the metallic enclosure [19]. The final transmission line lengths and widths are summarised in Table 4.7 and the modelled filter with the enclosure is depicted in Figure 4.10. The simulation included the SMA connectors, where the launch grounding is via the enclosure to the circuit.

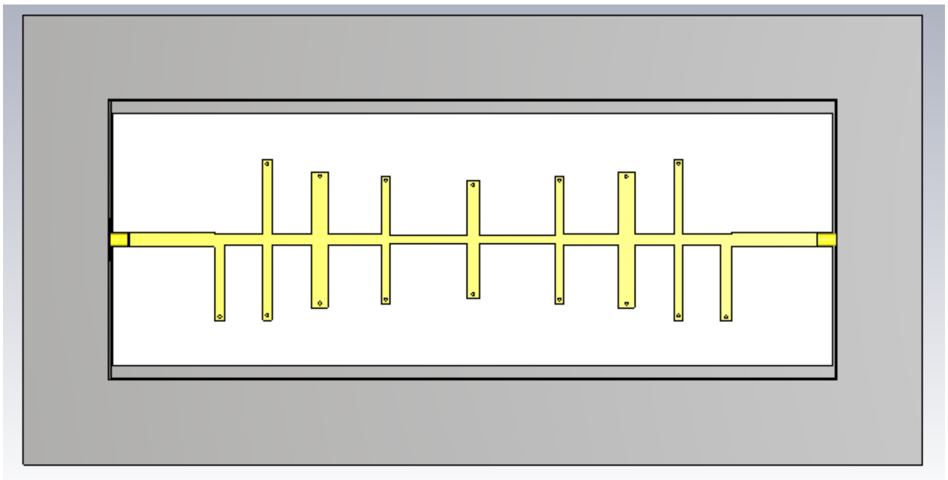

Figure 4.10: 3D Model with enclosure of the designed bandpass filter.

The simulated result of the modelled filter structure inside the enclosure is depicted in Figure 4.11 where an improved return loss can be seen when compared to the simulated result without the enclosure, represented by the dotted trace. This is largely attributed to the optimised length and width of the 50 Ω coupling feed lines.

Table 4.7: Optimised EM microstrip structure line lengths and widths with enclosure

Transmission Line	**Width (mm)**	**Length (mm)**
TL1, TL17	1.02	8.74
TL3, TL15, TL19, TL25	0.89	8.095
TL5, TL13, TL20, TL24	1.68	6.85
TL7, TL11, TL21, TL23	0.86	6.425
TL9, TL22	1.30	5.955
TL2, TL16	1.08	3.83
TL4, TL14	1.10	3.99
TL6, TL12	1.05	5.41
TL8, TL10	0.80	7.66

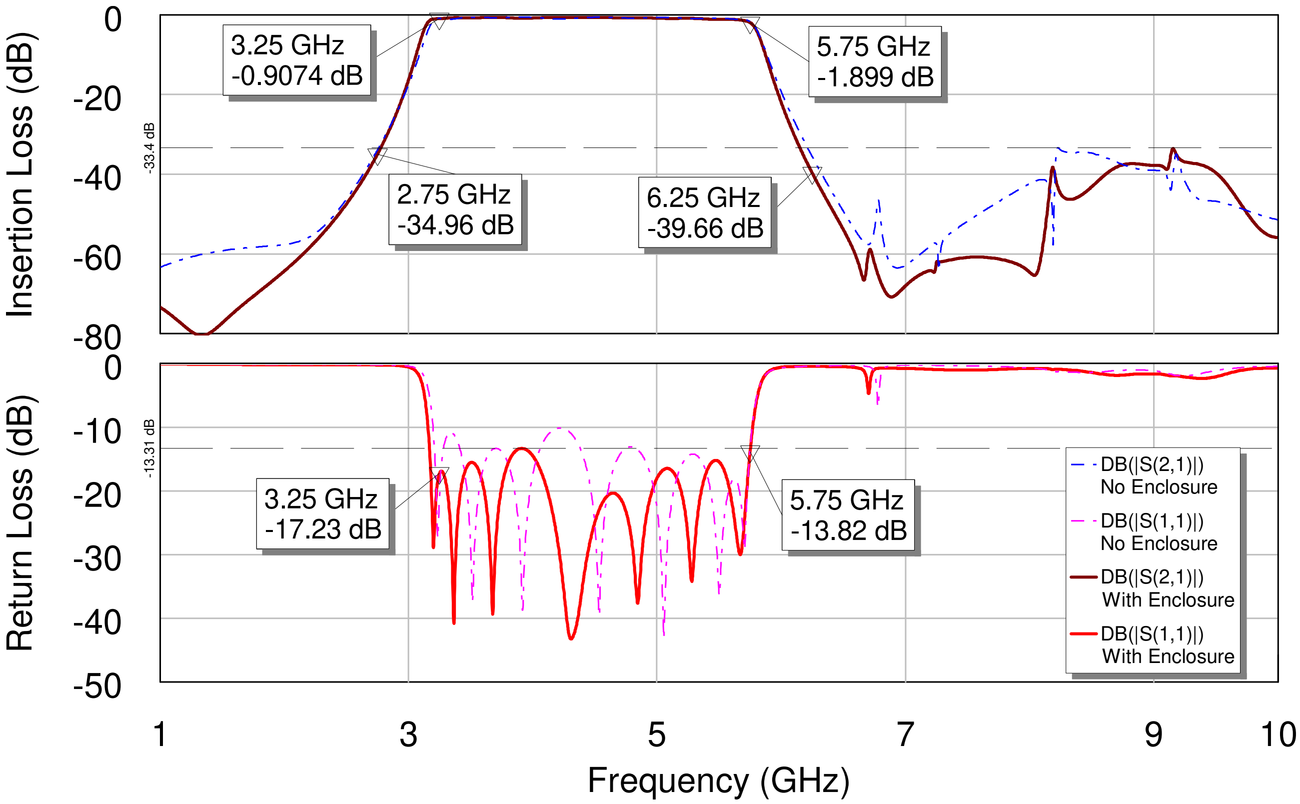

Figure 4.11: EM Simulation plot of the designed bandpass filter with enclosure.

A slightly improved out-of-band rejection can also be observed, where upper passband transition is slightly steeper with the enclosure as opposed to without the enclosure. It should be noted that although there exists a spurious harmonic centered around $2\omega_0$, the overall out-of-band rejection from 6.25 GHz to 10 GHz is better than 30 dB, which meets the specifications. Therefore no further intervention is required to improve the design.

4.5 Circuit Layout and Measurements

The optimised circuit dimensions was then exported to Altium Designer [64], a PCB design software package, where the PCB was prepared for manufacturing. The final PCB layout is depicted in Figure 4.12 where the stub short circuiting vias were modelled as through-hole plated vias having a diameter of 0.3 mm.

The manufactured PCB was integrated into the enclosure (top in Figure 4.13) and connectorised using female (jack) SMA panel mount connectors. The populated structure was then measured using the Rohde & Schwarz ZVA40 Vector Network Analyzer (VNA).

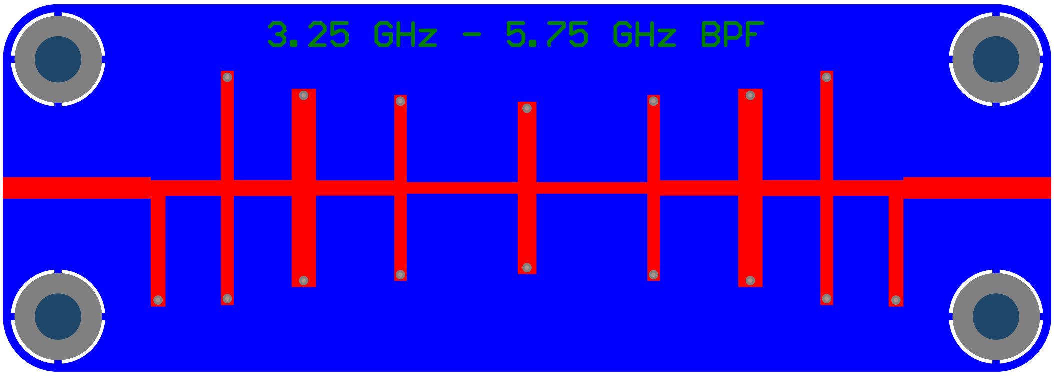

Figure 4.12: PCB Layout of the designed bandpass filter.

It can be seen from the measurement results plotted in Figure 4.14 that it does not quite correlate with the simulated results. The performance parameters measured which are most divergent from the simulated results are the passband return loss, and the out-of-band rejection. Each of these will be addressed individually in the subsequent sub-sections.

4.5.1 Measured Return Loss

The return loss over the band was simulated as 13.31 dB, yet the measurement yielded a worst case result of 8.34 dB over the band (pink trace in Figure 4.14), which does not meet the specification of $\geq$ 10 dB.

This result discrepancy can be mainly attributed to grounding inadequacies caused by the combination of the enclosure and the SMA panel mount connectors. The enclosure was modelled in CST as a Perfect Electrical Conductor (PEC), which creates a perfect boundary environment such that the boundary unions form a closed loop for the current path. However, the realised enclosure is not as "perfect" as the model, where adequate grounding of the shunt stubs for this filter topology is imperative to its performance. To validate this hypothesis, the manufactured filter was connectorised outside of the enclosure, where edge mount SMA connectors were used (bottom in Figure 4.13). The ground tab of the SMA connectors were soldered onto the underside of the PCB, namely the ground plane, thereby ensuring a solid ground connection at the launch.

From the measurement results in Figure 4.14, it can be seen that the return loss over the band (black trace in Figure 4.14) now correlates well with the simulated result when the ground connection is directly connected to the circuit ground-plane, where it achieved a worst case result of approximately 12.83 dB. This experiment therefore validates the hypothesis that the combination of the enclosure and panel mount SMA connectors provides insufficient

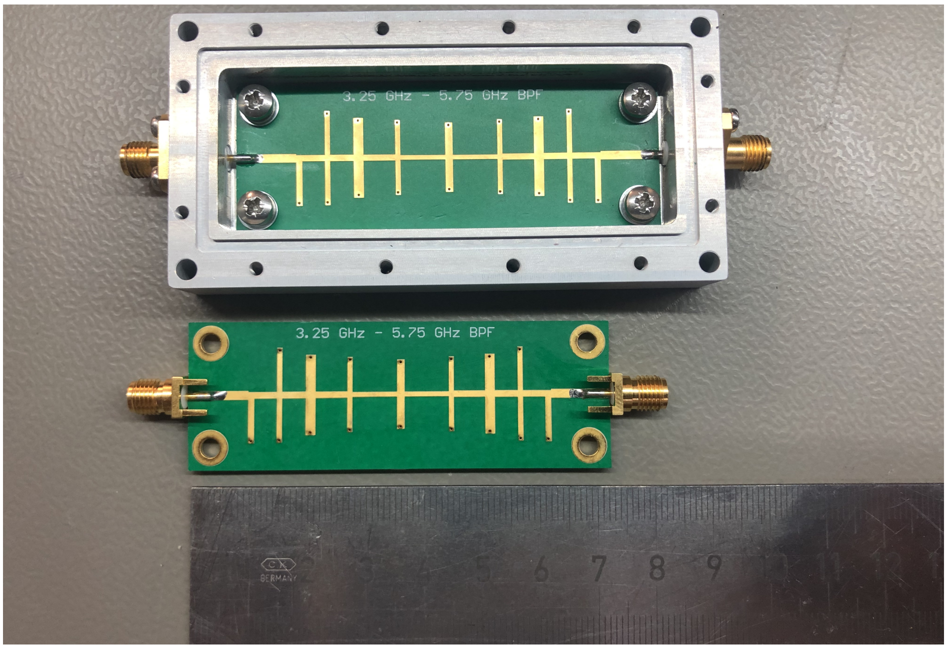

Figure 4.13: Manufactured PCB with and without enclosure.

grounding, thereby adversely affecting the return loss over the band. Figure 4.15 depicts a close-up view of the measured passband ripple with and without the enclosure.

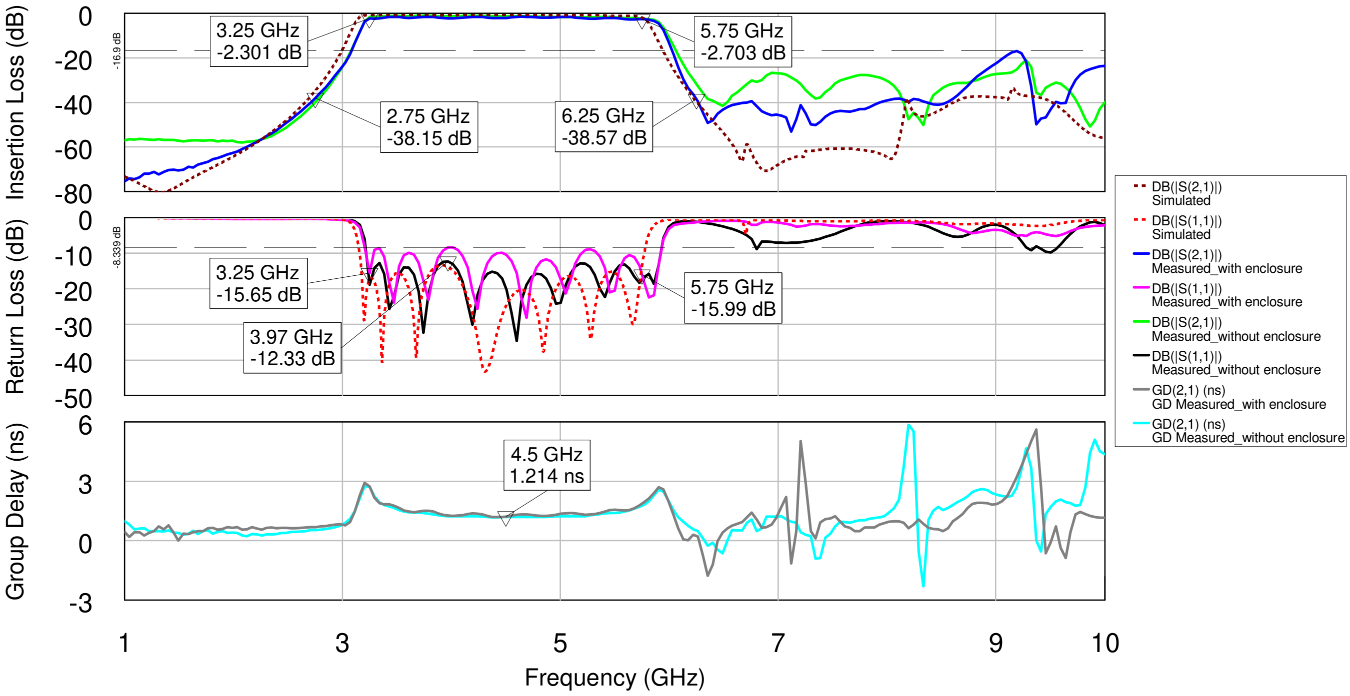

Figure 4.14: Comparison of measured results.

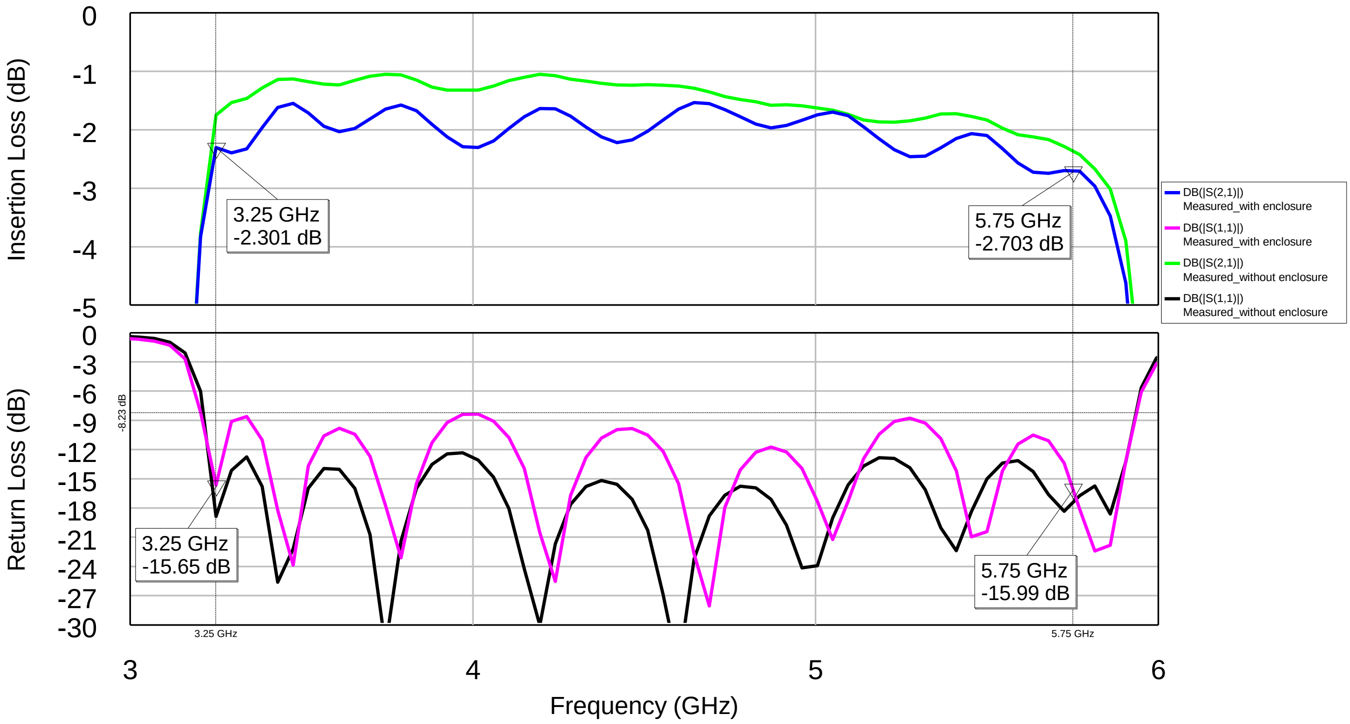

Figure 4.15: Passband ripple comparison of measured results.

4.5.2 Measured Out-of-band Rejection

From figure 4.14 it can be seen that the measured out-of-band rejection, represented by the blue trace, depicts a prominent spurious harmonic prevalent at around $2f_0$, with the peak being at approximately at 9.2 GHz with an attenuation of -16.9 dB. The simulated result (dotted brown trace in Figure 4.14) however indicated that this spurious harmonic was expected to be better than -30 dB.

Matthaei *et al.* [21] suggests that this filter topology, despite being very suitable for wideband applications, is prone to having a narrow spurious harmonic in the proximity of $2f_0$, which is caused by the slightest dimensional inaccuracies of the stubs.

To validate this notion, a Yield Analysis which makes use of the Monte Carlo analysis, of the circuit design in Figure 4.7 was done using AWR. The analysis applies statistical variations on the circuit components in order to obtain it's effects on the circuit performance.

The dimensional inaccuracies is a consequence of the tolerances applied by the PCB manufacturer. Hence for this experiment, the statistical analysis distribution of the simulation was configured to have a standard deviation or tolerance of 10%, which was applied to each stub width dimension. The Yield Goal amplitude value was set as -23 dB, as per the specification.

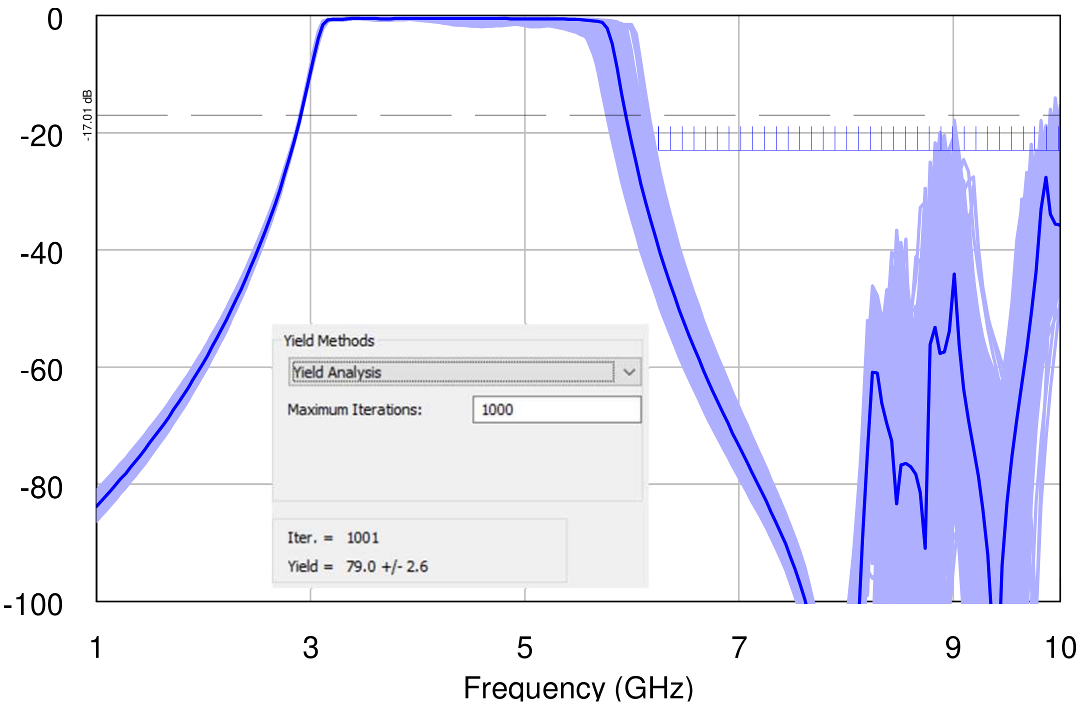

Yield Analysis
Maximum Iterations: 1000
Iter. = 1001
Yield = 79.0 +/- 2.6

Figure 4.16: Yield Analysis simulation result.

The Yield Analysis simulation result is depicted in Figure 4.16, where it can be seen that when a dimensional tolerance of 10% is applied to the width dimension of the interior stubs, the influences is largely on the position and amplitude of the spurious harmonic. The analysis also shows a worst case result of -17 dB, which correlates well with measured result in Figure 4.14.

The analysis simulation result also indicates that the expected yield is approximately 79%, which suggests there is a likelihood that 21% of the manufactured batch of PCBs may have a spurious harmonic with an amplitude of $\geq$ -23 dB if a 10% manufacturing tolerance is applied.

These effects can be mitigated against in future by performing a yield optimisation simulation prior to manufacturing. The simulation would optimise the circuit yield by modifying the nominal values of the width dimension of the interior stubs, thereby increasing the probability for a larger manufactured yield.

Based on this it can be concluded the likely reason for the out-of-band rejection amplitude discrepancy is due to dimensional inaccuracies associated with the PCB fabrication.

Chapter 5

Conclusions and Recommendations

5.1 Conclusions

The objective of this thesis was to design and build a planar bandpass filter having a bandwidth of 2.5 GHz, centered around 4.5 GHz. Furthermore, the designed filter should meet the performance specifications summarised in Table 1.1. These performance specifications have been derived in [2] and [3] in such a manner that the designed filter would be suited for use with digitisers capable of sampling at 6 Gsps.

Various literature sources were consulted in order to obtain a list of suitable filter topologies capable of achieving the performance specifications. Each topology applicable to this application was evaluated based on the set of given specifications. Based on the evaluations, it was decided that the $\lambda_g/4$ shunt short-circuited stub bandpass filter implemented on microstrip would be best suited to meet the design specifications whilst maintaining a moderately compact circuit size.

An evaluation revealed that a 9^{th} Order Chebyshev bandpass filter having a passband ripple of 0.01 dB would be best suited for this application. The theoretical design was done by using closed-form formulae, and then modelled using the commercial CAD package, AWR.

The circuit simulation results showed good agreement with design objectives. An EM simulation of the 3D modelled design was then done using CST, where an enclosure was added in order to enhance the electrical and mechanical characteristics of the design. The EM simulation results were still in good agreement of the design objective, where an out-of-band rejection of $\geq$ 30 dB up to 10 GHz and return loss of 13.3 dB over the band from 3.25 - 5.75 GHz was achieved. The final optimised 3D model design was then exported to a PCB design software package, Altium Designer, where it was readied for manufacturing.

The measured results of the manufactured filter correlated in part to the simulated results. A summary of the simulated and measured results is presented in Table 5.1. The filter achieved the stopband attenuation requirement at 2.75 GHz and 6.25 GHz of $\geq$ 23 dB, but achieved an insertion loss at the band edges of 2.3 dB and 2.7 dB respectively.

Furthermore, the measured result of the passband return loss and the out-of-band rejection revealed discrepancies when compared to the simulated results. After analysis and investigation, it became evident that the combination of the enclosure and choice of connector attributed the poor return loss of 8.3 dB. This was proven by experimentation where the filter PCB was removed from the enclosure and connectorised with end-launch SMA connectors, with the ground tab of the connector firmly soldered onto the ground-plane of the PCB. The return loss result now correlated well with the simulated result, where the worst case return loss over the passband was measured as 12.33 dB.

The discrepancy relating to the out-of-band rejection was addressed by means of a Yield Analysis simulation. It has been reported by [21] that the performance of this filter topology is somewhat susceptible to mistuning, which causes the spurious harmonic at $2\omega_0$ to become more prominent. This notion was validated by the result of the Yield Analysis, where a 10% manufacturing tolerance was applied to the width dimension of the interior stubs. The simulation result plot showed that with this manufacturing tolerance applied, the spurious harmonic at $2\omega_0$ is largely affected.

The designed filter, despite not achieving all the specifications, has achieved a FBW of 55.6% whilst occupying a compact overall circuit size of 72.39 x 16.19 mm.

Table 5.1: Summary of performance results

Parameter	**Specification**	**Simulated**	**Measured**	
			With Enclosure	**Without Enclosure**
Upper Passband	5.75 GHz	5.75 GHz	5.75 GHz	5.75 GHz
Lower Passband	3.25 GHz	3.25 GHz	3.25 GHz	3.25 GHz
Bandwidth	2.5 GHz	2.5 GHz	2.5 GHz	2.5 GHz
Insertion Loss	$\leq$ 2 dB	1.899 dB	2.7 dB	2.36 dB
Return Loss	$\geq$ 10 dB	13.31 dB	8.34 dB	12.33 dB
Fractional Bandwidth	55.6 %	55.6 %	55.6 %	55.6 %
Lower Stopband attenuation	$\geq$ 23 dB	34.96 dB	$\geq$ 38 dB	$\geq$ 38 dB
Upper Stopband attenuation	$\geq$ 23 dB	39.66 dB	$\geq$ 23 dB up to 9 GHz	$\geq$ 23 dB up to 9.23 GHz

5.2 Recommendations and Future Work

On account of the designed filter not achieving all of the specifications given in Table 1.1, some improvements of the design is recommended for future work, such as:

- Improvement of circuit grounding

  The experiment conducted in Chapter 4 validated that inadequate grounding for this filter topology contributed to the poor return loss. The grounding can be improved by adding additional PCB mounting holes, thus ensuring even contact to the enclosure surface and thereby improving the grounding.

  Another consideration might be to re-design the metallic enclosure in order to accommodate a different type of SMA connector, one which is capable of grounding directly to the PCB ground-plane, and not through the enclosure.

- Filter design cascaded with a low-pass filter

  The measured result of the designed filter depicts a prominent spurious harmonic centered around $2\omega_0$ due to the mistuning of the stubs owing to fabrication tolerances. These tolerances are somewhat unavoidable, therefore it is proposed that the design incorporate a cascaded low-pass filter to ensure that the spurious harmonic is sufficiently attenuated. In order to maintain a compact overall circuit size, it could be attempted to embed the low-pass filter with the designed bandpass filter, such as those described in Chapter 3.

- "Via-less" short-circuited stubs

  During the design it was found that the connection of the short-circuited shunt stubs to ground using vias has significant impact on the circuit return loss. It is proposed that the next iteration of the design explore an alternative method to grounding the short-circuited stubs, namely a "via-less" design, which is expected to reduce the overall circuit loss and effects caused by the vias.

References

[1] J. Condon and S. Ransom, *Essential Radio Astronomy*, ser. Princeton Series in Modern Observational Astronomy. Princeton University Press, 2016.

[2] J. A. Malan, “X-band Digitization Systems Aspects and Filters for MeerKAT Radio Astronomy Receiver,” Master’s thesis, University of Cape Town, 2017.

[3] S. Mundia, “Concept Demonstrator for MeerKAT Operation from 14.5 to 20 GHz,” Master’s thesis, University of Cape Town, May 2019.

[4] SARAO MeerKAT. [Online]. Available: https://www.sarao.ac.za/science/meerkat/about-meerkat/ (Accessed 2021-02-15).

[5] SKA Public. [Online]. Available: http://public.ska.ac.za/meerkat (Accessed 2021-02-15).

[6] “Meerkat.” [Online]. Available: https://www.sarao.ac.za/gallery/meerkat/ (Accessed 2021-03-02).

[7] MeerKAT Factsheet, 2016. [Online]. Available: https://www.sarao.ac.za/wp-content/uploads/2016/07/meerkat-fact-sheet-2016.pdf (Accessed 2021-02-15).

[8] R. Braun, A. Bonaldi, T. Bourke, E. Keane, and J. Wagg, “Anticipated Performance of the Square Kilometre Array - Phase 1 (SKA1).” [Online]. Available: https://arxiv.org/ftp/arxiv/papers/1912/1912.12699.pdf (Accessed 2021-12-02).

[9] “SKA1 MID Poster.” [Online]. Available: https://www.skatelescope.org/wp-content/uploads/2018/07/13572_SKA-poster-resize_MID1-1.pdf (Accessed 2021-12-02).

[10] S. Malan, “Casper workshop 2017.” [Online]. Available: http://www.tauceti.caltech.edu/casper-workshop-2017/slides/11_malan.pdf (Accessed 2021-06-12).

[11] e2v ADC Product Datasheet, “EV12AQ600 Quad 12-bit 1.6 GSps ADC with embedded cross-point switch , Digitizing up to 6.4 GSps,” Teledyne e2v Semiconductors, pp. 1–131, June 2020. [Online]. Available: https://www.teledyne-e2v.com/products/semiconductors/adc/ev12aq600/ (Accessed 2021-02-15).

[12] W. Kester, *Data Conversion Handbook*, ser. Analog Devices series. Elsevier Science, 2005.

[13] P. Poshala, "Why oversample when undersampling can do the job?" [Online]. Available: https://www.ti.com/lit/an/slaa594a/slaa594a.pdf (Accessed 2022-01-11).

[14] T. J. Rouphael, *RF and Digital Signal Processing for Software-Defined Radio.* Newnes, 2009.

[15] J. H. Reed, *Software radio: a modern approach to radio engineering.* Prentice Hall Professional, 2002.

[16] F. Maloberti and A. C. Davies, *A Short History of Circuits and Systems.* River Publishers, 2016.

[17] G. C. Temes and S. K. Mitra, *Modern Filter Theory and Design.* Wiley, 1973.

[18] D. M. Pozar, *Microwave Engineering*, 4th ed. United States of America: John Wiley & Sons, Inc., 2012.

[19] J.-S. Hong, *Microstrip Filters for RF/Microwave Applications*, 2nd ed. Hoboken, NJ, USA: John Wiley & Sons, Inc., 2011.

[20] R. Saal and E. Ulbrich, "On the Design of Filters by Synthesis," *IRE Transactions on Circuit Theory*, vol. 5, no. 4, pp. 284–327, 1958.

[21] G. L. Matthaei, L. Young, and E. M. T. Jones, *Microwave filters, impedance-matching networks, and coupling structures.* NJ, USA: Artech House, nov 1980.

[22] L. Zhu, S. Sun, and R. Li, *Microwave Bandpass Filters for Wideband Communications*, ser. Wiley Series in Microwave and Optical Engineering. Wiley, 2012.

[23] C. Bowick, *RF circuit design, 2nd ed.* Newnes, 2008.

[24] I. Bahl, *Lumped Elements for RF and Microwave Circuits*, ser. Artech House microwave library. Artech House, 2003.

[25] H. A. Wheeler, "Transmission-line properties of parallel wide strips by a conformal-mapping approximation," *IEEE Transactions on Microwave Theory and Techniques*, vol. 12, pp. 280–289, 1964.

[26] H. A. Wheeler, "Transmission-line properties of parallel strips separated by a dielectric sheet," *IEEE Transactions on Microwave Theory and Techniques*, vol. 13, pp. 172–185, 1965.

[27] E. Hammerstad, “Equations for microstrip circuit design,” in *1975 5th European Microwave Conference*, 1975, pp. 268–272.

[28] M. Makimoto and S. Yamashita, *Microwave Resonators and Filters for Wireless Communications: theory, design and application.* Springer, 2001.

[29] Z. Hao and J. Hong, “Ultrawideband filter technologies,” *IEEE Microwave Magazine*, vol. 11, no. 4, pp. 56–68, 2010.

[30] T.-N. Kuo, S.-C. Lin, and C. Chen, “Compact ultra-wideband bandpass filters using composite microstrip–coplanar-waveguide structure,” *IEEE Transactions on Microwave Theory and Techniques*, vol. 54, no. 10, pp. 3772–3778, 2006.

[31] P. Cai, Z. Ma, X. Guan, Y. Kobayashi, T. Anada, and G. Hagiwara, “A novel compact ultra-wideband bandpass filter using a microstrip stepped-impedance four-modes resonator,” in *2007 IEEE/MTT-S International Microwave Symposium*, 2007, pp. 751–754.

[32] Z.-C. Hao and J.-S. Hong, “Ultra-wideband bandpass filter using multilayer liquid-crystal-polymer technology,” *IEEE Transactions on Microwave Theory and Techniques*, vol. 56, no. 9, pp. 2095–2100, 2008.

[33] W. Menzel, M. Rahman Tito, and L. Zhu, “Low-loss ultra-wideband (uwb) filters using suspended stripline,” in *2005 Asia-Pacific Microwave Conference Proceedings*, vol. 4, 2005, pp. 2148–2151.

[34] C.-W. Tang and M.-G. Chen, “A microstrip ultra-wideband bandpass filter with cascaded broadband bandpass and bandstop filters,” *IEEE Transactions on Microwave Theory and Techniques*, vol. 55, no. 11, pp. 2412–2418, 2007.

[35] M. Kheir, *UWB Technology: Circuits and Systems.* IntechOpen, 2020.

[36] “Revision of part 15 of the commission’s rules regarding ultra wideband transmission systems,” Washington DC, Apr 2002. [Online]. Available: https://www.fcc.gov/document/revision-part-15-commissions-rules-regarding-ultra-wideband-7

[37] Zhou Tie, Qu Dexin, Wang Junhui, and Huang Xing, “A noval microstrip ultra-wide bandpass filter with highpass filter and lowpass filter,” in *2008 8th International Symposium on Antennas, Propagation and EM Theory*, 2008, pp. 1354–1357.

[38] Ching-Luh Hsu, Fu-Chieh Hsu, and J.-K. Kuo, “Microstrip bandpass filters for ultra-wideband (uwb) wireless communications,” in *IEEE MTT-S International Microwave Symposium Digest, 2005.*, 2005, pp. 679–682.

[39] L. Zhu, H. Bu, and K. Wu, "Aperture compensation technique for innovative design of ultra-broadband microstrip bandpass filter," in *2000 IEEE MTT-S International Microwave Symposium Digest (Cat. No.00CH37017)*, vol. 1, 2000, pp. 315–318 vol.1.

[40] L. Zhu, S. Sun, and W. Menzel, "Ultra-wideband (uwb) bandpass filters using multiple-mode resonator," *IEEE Microwave and Wireless Components Letters*, vol. 15, no. 11, pp. 796–798, 2005.

[41] H. Wang and L. Zhu, "Aperture-backed microstrip line multiple-mode resonator for design of a novel uwb bandpass filter," *2005 Asia-Pacific Microwave Conference Proceedings*, vol. 4, pp. 4–, 2005.

[42] M. C. Velazquez-Ahumada, J. Martel, and F. Medina, "Parallel coupled microstrip filters with ground-plane aperture for spurious band suppression and enhanced coupling," *IEEE Transactions on Microwave Theory and Techniques*, vol. 52, pp. 1082–1086, 2004.

[43] A. M. Abbosh, "Design method for ultra-wideband bandpass filter with wide stopband using parallel-coupled microstrip lines," *IEEE TRANSACTIONS ON MICROWAVE THEORY AND TECHNIQUES*, vol. 60, pp. 31–38, 2012.

[44] M. K. Khandelwal, B. K. Kanaujia, and S. Kumar, "Defected ground structure: Fundamentals, analysis, and applications in modern wireless trends," *International Journal of Antennas and Propagation*, pp. 1–22, 2017.

[45] Jong-Im Park, Chul-Soo Kim, Juno Kim, Jun-Seok Park, Yongxi Qian, Dal Ahn, and T. Itoh, "Modeling of a photonic bandgap and its application for the low-pass filter design," in *1999 Asia Pacific Microwave Conference. APMC'99. Microwaves Enter the 21st Century. Conference Proceedings (Cat. No.99TH8473)*, vol. 2, 1999, pp. 331–334 vol.2.

[46] G. Breed, "An introduction to defected ground structures in microstrip circuits," *High Frequency Electronics*, vol. 7, no. 11, pp. 50–54, 2008.

[47] L. H. Weng, Y. chun Guo, X. wei Shi, and X. Chen, "An overview on defected ground structure," *Progress in Electromagnetics Research B*, vol. 7, pp. 173–189, 2008.

[48] W. Tang, S. Yang, X. Wang, C. Wang, and Y. L. Chow, "A novel uwb bandpass filter using highpass and lowpass filters," in *2012 4th International High Speed Intelligent Communication Forum*, 2012, pp. 1–2.

[49] R. Levy, R. Snyder, and G. Matthaei, "Design of microwave filters," *IEEE Transactions on Microwave Theory and Techniques*, vol. 50, no. 3, pp. 783–793, 2002.

[50] L. G. Maloratsky, “Reviewing the basics of suspended striplines,” *Microwave Journal*, vol. 45, pp. 82–98, 2002.

[51] A. Balalem, W. Menzel, J. Machac, and A. Omar, “A simple ultra-wideband suspended stripline bandpass filter with very wide stop-band,” *IEEE Microwave and Wireless Components Letters*, vol. 18, no. 3, pp. 170–172, 2008.

[52] V. Palazzari, S. Pinel, M. M. Tentzeris, L. Roselli, J. Laskar, and F. Alimenti, “Design of wlan filters in ltcc and lcp system-on-package technologies.” German Microwave Conf, 2005.

[53] Z.-C. Hao and J.-S. Hong, “Developing compact wideband filters using multilayer liquid crystal polymer technology,” in *2015 Asia-Pacific Microwave Conference (APMC)*, vol. 2, 2015, pp. 1–3.

[54] Z.-C. Hao and J.-S. Hong, “Uwb bandpass filter using cascaded miniature high-pass and low-pass filters with multilayer liquid crystal polymer technology,” *IEEE Transactions on Microwave Theory and Techniques*, vol. 58, no. 4, pp. 941–948, 2010.

[55] N. Kingsley, “Liquid crystal polymer: Enabling next-generation conformal and multilayer electronics,” *Microwave Journal*, vol. 51, pp. 188–200, 05 2008.

[56] DuPont Microcircuit Materials, “Cost-effective solutions for high density interconnect and rf modules using low temperature cofired ceramic materials,” apr 2001. [Online]. Available: https://www.microwavejournal.com/articles/3177-cost-effective-solutions-for-high-density-interconnect-and-rf-modules-using-low-temperature-cofired-ceramic-materials (Accessed 2021-12-06).

[57] C.-W. Tang and D.-L. Yang, “Realization of multilayered wide-passband bandpass filter with low-temperature co-fired ceramic technology,” *IEEE Transactions on Microwave Theory and Techniques*, vol. 56, no. 7, pp. 1668–1674, 2008.

[58] L. G. Maloratsky, “Design and technology tradeoffs in passive rf and microwave integrated circuits,” *High Frequency Electronics*, pp. 40–54, 2010. [Online]. Available: http://www.highfreqelec.summittechmedia.com/Sep10/HFE0910_Maloratsky.pdf

[59] AWR v16, “AWR Design Environment,” Cadence. [Online]. Available: https://www.awr.com/awr-software/products/awr-design-environment

[60] Rogers RT/duroid 6006/6010LM Product Datasheet, “RT/duroid 6006/6010LM - High Frequency Laminates,” Rogers Corporation, pp. 1–2, 2020. [Online]. Available: https://rogerscorp.com/advanced-electronics-solutions/rt-duroid-laminates/rt-duroid-6006-and-6010-2lm-laminates (Accessed 2021-06-28).

[61] D. Swanson, “Grounding microstrip lines with via holes,” *IEEE Transactions on Microwave Theory and Techniques*, vol. 40, no. 8, pp. 1719–1721, 1992.

[62] CST 2021, “Computer simulation technology (CST),” Dassault Systems. [Online]. Available: https://www.3ds.com/products-services/simulia/products/cst-studio-suite/

[63] 3ds, “Microwave filters and RF components: EM simulation, Electromagnetic Solver Technology for Filters and Components,” Dassault Systems. [Online]. Available: https://www.3ds.com/products-services/simulia/products/electromagnetic-simulation/microwave-filter-applications/

[64] Altium v21, “Altium Designer.” [Online]. Available: https://www.altium.com/altium-designer/